CHALMERS
UNIVERSITY OF TECHNOLOGY

Particle/Antiparticle Nature of Light Dark Matter in Direct Detection

Discrimination between Dirac and Majorana Dark Matter through Probing the Scattering off Electrons

Master's thesis in Physics and Astronomy

Julia Ravanis

Department of Physics
Chalmers University of Technology
Gothenburg, Sweden 2019

Master's thesis 2019:NN

Particle/Antiparticle Nature of Light Dark Matter in Direct Detection

Discrimination between Dirac and Majorana Dark Matter through Probing the Scattering off Electrons

JULIA RAVANIS

CHALMERS
UNIVERSITY OF TECHNOLOGY

Department of Physics
Division of Subatomic and Plasma Physics
Chalmers University of Technology
Gothenburg, Sweden 2019

Discrimination between the Dirac and Majorana nature of sub-GeV dark matter, based on the dark matter-electron scattering in direct detection experiments.
JULIA RAVANIS

Supervisor: Riccardo Catena, Assistant Professor, Subatomic and Plasma Physics
Examiner: Gabriele Ferretti, Professor, Subatomic and Plasma Physics

Master's Thesis 2019:NN
Department of Physics
Division of Subatomic and Plasma Physics
Chalmers University of Technology
SE-412 96 Gothenburg
Telephone +46 31 772 1000

Typeset in LaTeX
Gothenburg, Sweden 2019

Abstract

In the last century, astronomers have concluded that the luminous mass in the Universe impossibly can be responsible for the huge gravitational pull observed in stellar and galactic systems. The explanation for this discrepancy between luminous mass and gravitational effects is believed to be dark matter – an unknown particle species that does not emit or absorb light at detectable wavelengths. Although extensive efforts have been made to detect this mysterious particle, it remains undiscovered, and its nature is one of the greatest unsolved questions in fundamental physics.

This thesis investigates the prospects of discriminating between Dirac and Majorana dark matter, if dark matter is to be found in direct detection experiments. The Dirac or Majorana nature of a particle corresponds to the existence or absence of a distinct antiparticle, which for the invisible, and therefore probably neutral, dark matter particle is a property of major importance. The theoretical framework is fermionic dark matter at the sub-GeV mass scale, interacting with electrons in direct detection experiments with argon, xenon and germanium targets. The coupling constant parameter space of photon mediated interactions is explored, and the regions where statistical rejection of a Majorana hypothesis could be possible in the future are determined.

It is found that the discrimination significance for rejecting a Majorana hypothesis, given simulated Dirac-like experimental signals, reaches values of >4 standard deviations for a substantial part of the coupling constant parameter space for germanium targets, whereas argon and xenon targets entail stronger restrictions on the discrimination parameter space. The discrimination significance is highly dependent on the available detection energy region, and the dark matter mass.

Key words: dark matter, Dirac, Majorana, direct detection, electron scattering.

Acknowledgements

I am grateful to my supervisor Riccardo Catena, the person who awoke my interest for dark matter, and who has helped me with everything from scattering amplitude derivations to Mathematica code troubleshooting, without ever getting tired of answering questions about physics. I would also like to thank Erik Johansson, with whom I shared an office and all the ups and downs a Master's thesis brings with it when written, Timon Emken and Vanessa Zema, from whom I learned a lot about the dark matter research field during our group meetings, and finally my other friends from Physics and Astronomy at Chalmers, that have enlightened me in areas ranging from string theory to politics, making the rainy workdays a bit brighter.

Julia Ravanis, Gothenburg, June 2019

Contents

1 Introduction

Ever since the 18th, century astronomers have been referring to dark matter in the sky when asking questions about the Universe [1]. These invisible objects were often believed to be stars or other known astronomical bodies, only too faint or too far away to be seen from Earth. It is only recently, in the past few decades, that the term "dark matter" has come to be the label of an unknown particle species, unable to emit or absorb light at measurable wavelengths but noticeably affecting its surroundings through gravity. However, the mystery embedded in the word "dark" – once just a description but nowadays a distinguished name – still prevails.

Although the evidence for the existence of dark matter in the Universe is overwhelming, the nature of dark matter is one of the great unsolved questions in astroparticle physics and in science in general. The solution could point towards new paths in cosmology, which would help us understand the past and future of our Universe, and perhaps even throw the so faithful but so frustrating Standard Model of particle physics over, once and for all.

This thesis is a contribution to the gigantic research project that aims to determine what dark matter is. Focus is on the particle/antiparticle nature of dark matter – a feature that could help single out which dark matter model is actually describing reality. If dark matter is its own antiparticle, which for fermions correspond to a Majorana particle, this could point towards the supersymmetric extensions of the Standard Model. If dark matter on the contrary has a distinct antiparticle, as Dirac fermions do, this could point towards asymmetric dark matter models.

The particle/antiparticle nature investigated in this thesis applies for dark matter in the MeV – GeV mass range, so called light dark matter. This is a collection of dark matter models that is currently gaining a lot of interest in the astroparticle physics community, since large parts of the underlying parameter space is unexplored but experiments aiming to explore it already exist. One promising experimental procedure is direct detection, where interactions between Milky Way dark matter and Standard Model particles are probed in low-background detectors. In the MeV-mass range, dark matter would primarly interact with electrons, thus giving rise to excitation signals in detector targets such as liquid noble gases or semiconductors [2]. Three distinct target materials will be considered in this project; argon, xenon and germanium.

The different signal event rates that are to be expected in these experiments if the dark matter particle is a Majorana or a Dirac fermion are calculated for the particle physics scenario of dark matter-electron scattering, mediated by a loop level photon interaction. Although dark matter does not emit or absorb measurable light, it can still interact with photons through higher-dimensional operators [3]. This theoretical framework is chosen after proving that spin independent, general couplings to electrons results in indistinguishable event rates. Through a statistical analysis of Monte Carlo simulated experimental data, it is shown that a Majorana hypothesis can be rejected in favour of a Dirac

hypothesis. Thus the possibility that dark matter is identical to its antiparticle can be excluded. This has been done within the experimental framework of dark matter-nuclei scattering [4], but not for electron scattering.

The statistical analysis of the particle/antiparticle nature of dark matter is crucial in the design optimisation of next generation direct detection experiments searching for sub-GeV dark matter – it can highlight the strengths and weaknesses of different experimental setups, and it can determine the prospects, in terms of number of signal events for different regions of the mass- and couplings parameter space, for future discoveries regarding the particle nature of dark matter.

1.1 Purpose

The main purpose of this thesis is to investigate the prospects for determining the particle/antiparticle nature of dark matter particles in the MeV–GeV mass range, interacting with electrons in direct detection experiments based upon argon, xenon and germanium. What parts of the interaction coupling parameter space enables discrimination between the Dirac and Majorana nature, and how big is this discrimination?

1.2 Thesis outline

The thesis begins with a background chapter, where an overview of the evidence for dark matter is given, as well as a description of the most relevant possible dark matter candidates, the current detection techniques and the particle/antiparticle nature. It is followed by a theoretical review, which treats the theory of Dirac fields and charge conjugation, needed to distinguish between Dirac and Majorana particles, and calculations of their corresponding signal event rates, based on dark matter-electron scattering in semiconductor and liquid noble gas detectors.

The numerical calculation procedure is then described in the next chapter, where the approximations used in the calculation are explained and motivated. Here the data simulation and the statistical analysis, used to discriminate between the two hypotheses, is also presented. This is followed by a presentation of the results. That is, the discrimination significance for rejection of the Majorana hypothesis, given a dark matter signal simulated under the Dirac hypothesis in the chosen theoretical framework, for a range of different free parameters. The three experimental setups are compared. Lastly, the results are discussed in light of the theoretical background, the uncertainties in the discrimination procedure and the future prospects of discovering dark matter.

2 Background

Although the word "dark" has been used for a long time to describe various amounts of objects in astronomy, the contemporary meaning of "dark matter" dates back to the early 1900s. In 1904, Lord Kelvin proposed a method to link the velocity dispersion of stars to the mass of the stellar system: gases of particles obey the laws of thermodynamics, so through describing stars as gas clouds one can induce the mass needed to maintain the observable movement of the stars [5]. The discrepancy between this mass and the luminous mass of the stars was baptised to dark matter.

Since then the evidence for this discrepancy between luminous mass and mass induced from gravitational effects on other observables has continued to grow, and it is now a well established scientific fact. The search for dark matter has evolved into an entire field of research, and the theoretical particle models of dark matter range from super light bosonic axions to super heavy "wimpzillas", intriguing scientists all over the world [6]. In the following sections, I will go through the major evidence for dark matter on different size scales, some of the possible candidates for dark matter, and the experimental procedures that aims to detect them. Finally, a short presentation of the particle/antiparticle nature of dark matter, and the prospects for determining it, will be given.

2.1 Evidence for dark matter

The evidence for dark matter ranges from interstellar scales, through galaxies and galaxy clusters to the largest cosmological structure. I will begin with the galactic scale, where rotation curves of spiral galaxies are the observables in question; continue with galaxy clusters, where the velocity dispersion of galaxies constitute the evidence; and finally discuss the evidence on the largest cosmological structure, focusing on temperature anisotropies in the cosmic microwave background radiation and structure formation. This section is to a large extent based upon the overview of particle dark matter by Bertone, Hooper and Silk from 2008 [7].

2.1.1 Galactic scale

On a galactic scale, the evidence for dark matter mainly comes from the relationship between circular velocities of stars and gas in spiral galaxies and their radial distance from the galactic centre – the so called rotation curves. The circular velocity of a star in a galaxy depends on the gravitational potential, which is linked to the mass of the galaxy. Thus the gravitational mass can be estimated from the circular velocities and compared to the luminous mass.

The inward acceleration a of matter rotating in the galactic plane, and the spherically symmetric

Newtonian gravitational potential, V, at distance r from the centre are

$$a(r) = \frac{v_c^2}{r} = \frac{\partial V(r)}{\partial r}, \quad V(r) = -\frac{GM(r)}{r}. \tag{2.1}$$

G is the gravitational constant, v_c is the circular velocity and $M(r)$ is the mass contained within a sphere of radius r with density distribution $\rho(r')$: $M(r) = 4\pi \int_0^r \rho(r')r'^2 dr'$. The relation between circular velocity and mass is therefore

$$v_c(r) = \sqrt{\frac{GM(r)}{r}}. \tag{2.2}$$

For large radii, the luminous density distribution ρ_L in a galaxy is approaching zero, leaving $M(r)$ constant. Therefore, one would expect to see the rotation curves fall off as $1/\sqrt{r}$ for large r. This is however not the case. The experimental data instead show rotation curves that are almost constant at large radii – they are flat instead of slowly decreasing. This is where the dark matter enters the stage; by introducing a dark matter halo, with density distribution $\rho_{DM} = C/r^2$ for some constant C, the flat curves are reproduced theoretically. The total mass distribution is then

$$M(r) = 4\pi \int_0^r (\rho_L + \rho_{DM})r'^2 dr' = M_{L,\text{const}} + 4\pi C r, \tag{2.3}$$

for r bigger than the radius of the visible stellar disc. This yields the rotation curve

$$v_c(r) = \sqrt{\frac{GM_{L,\text{const}}}{r} + G4\pi C}. \tag{2.4}$$

By adjusting the constant C, the term stemming from the dark matter halo can compensate for the $1/\sqrt{r}$-dependence, leaving the rotation curve flat and thus reestablishing the connection between observations and Newtonian gravity. It is however hard to estimate the amount of dark matter through this approach, since it is difficult to measure how far the dark matter halo extends.

2.1.2 Galaxy clusters

The first evidence of dark matter on the next size scale, that of galaxy clusters, is one of the most famous results in dark matter history. In 1933, the Swiss-American astronomer Fritz Zwicky calculated the mass of the Coma cluster from the observed velocity dispersion of eight galaxies using the virial theorem, and found a discrepancy between the luminous and non-luminous mass corresponding to a mass-to-light ratio of a couple of hundreds [8].

The virial theorem states that the kinetic energy T and the potential energy V of a galaxy cluster must obey $2T + V = 0$, if the cluster is to be stable. Through expressing the kinetic and potential energies as averages over distances between the included galaxies, $\langle r \rangle$, and their velocity dispersion,

$\langle v^2 \rangle$, one can obtain a relation between the total mass M and the measurable velocities:

$$T = \frac{M\langle v^2 \rangle}{2}, \quad V = -\frac{GM^2}{2\langle r \rangle}, \quad \Longrightarrow M = \frac{2\langle v^2 \rangle \langle r \rangle}{G}. \tag{2.5}$$

It was this mass that Zwickey found to be much larger than the total luminous mass, found for example by counting the galaxies in the cluster and assuming an average mass for each.

Today the mass of galaxy clusters can be determined not only through Zwickey's method, but also from weak gravitational lensing, and from the X-ray emission profile tracing the distribution of hot intracluster gas. In general relativity, strong gravitational fields bend the lines along which light travels, thus distorting the images reaching us from behind heavy objects. The gravitational potential from a galaxy cluster can therefore be estimated from the distortion of background objects, and thereby the cluster mass can be induced. The X-ray emission estimation of cluster mass is instead based on thermodynamics. Assuming that the intracluster gas behaves like a spherically symmetric ideal gas, the equation for hydro-static equilibrium relating density to pressure can be expressed in terms of mass and temperature instead. This enables a calculation of galaxy cluster mass based on temperature determinations from X-ray emission profiles.

The observed temperature outside the core of galaxy clusters is substantially larger than the temperature expected for the luminous mass, pointing towards the existence of a large amount of dark matter in galaxy clusters. Weak gravitational lensing yields the same result, although this method has received some critique: the distribution of dark matter on galaxy cluster scale might be affected by the ordinary, baryonic matter distribution in unforeseen ways, leaving the results uncertain [9].

2.1.3 Large cosmological structures

The most convincing evidence for dark matter comes from the largest size scale in the Universe: surveys of the large scale cosmological structure and measurements of the temperature anisotropies in the cosmic microwave background radiation (CMB). It is also from the CMB analysis that the actual quantity of dark matter present in our Universe is conceived.

The overall cosmological structure origins from the early days of the Universe [10]. During the first $\sim$ 300 000 years after Big Bang, the Universe was very hot. The temperature was so high that electrons and protons were unable to combine into neutral atoms, leaving the matter content as a chaotic, shapeless plasma. This plasma interacted continuously with electromagnetic radiation, prohibiting light from travelling over any substantial distances. It was first when the temperature decreased to the point where neutral hydrogen could be formed, that light could escape from the scene and structure formation could begin. This is called the recombination, and the light emanating from this time period is called the cosmic microwave background radiation.

The problem – or for one who argues that dark matter exists the key – is that recombination occurs

too late to explain the structures we observe in the Universe today. When the evolution of the large scale structures are traced backwards in time, we land in the era of the hot particle plasma, where leptons and baryons were running wild, constantly flirting with light and therefore unable to build up the foundations of galaxies. The existence of dark matter in the early Universe could be the solution to this. Dark matter, weakly or not at all interacting with other Standard-Model particles and therefore untouched by their realm of chaos, could have formed the first structures in the Universe, around which the baryonic matter content later gathered. For this to be theoretically plausible however, dark matter needs to have been non-relativistic during structure formation [11]. This theory goes under the name Cold Dark Matter (CDM), often prolonged ΛCDM to also take Einstein's cosmological constant Λ into account. In contrast to relativistic Hot Dark Matter (HDM), ΛCDM is considered the most reliable cosmological model.

The other major argument for the existence of dark matter on the largest possible scale comes from the fluctuations in the CMB temperature. The CMB temperature is astonishingly homogeneous at about 2.7K, but it does exhibit fluctuations of order of magnitude 10^{-5} [7]. The angular dependence of these fluctuations can be expanded in terms of spherical harmonics $Y_{lm}(\theta, \phi)$:

$$\frac{\delta T}{T}(\theta, \phi) = \sum_{l=2}^{\infty} \sum_{m=-l}^{l} a_{lm} Y_{lm}(\theta, \phi). \tag{2.6}$$

The variance C_{lm} of the coefficients a_{lm}, $C_{lm} =< |a_{lm}|^2 >$, can be expressed as a function of l and plotted in what is called a CMB power spectrum. This function $C_{lm}(l)$ will theoretically depend on the solutions of Einstein's equations of general relativity at recombination, and therefore depend on the density variables Ω_b and Ω_M, describing the baryon density and the total matter density in the Universe. The likelihood of generating a model that fits the experimental temperature fluctuations data is optimised over all cosmological parameters, thereby extracting the most probable ratios of baryonic matter to total matter [12].

In figure 1, a CMB power spectrum showing both observed data and the best fitted theoretical model is presented. This is a ΛCDM model with specified densities – thus proving the existence of dark matter quantitatively. In order for the second peak in the spectrum to be present, a strict limit is put on the baryonic matter density, demanding that the majority of the matter content in the Universe is something other than baryons. The 2018 results from the Planck satellites are $\Omega_b h^2 \sim 0.02$ and $\Omega_M h^2 \sim 0.12$, where h is the Hubble constant [13]. Hence the conclusion: non-baryonic dark matter constitutes about 85% of all matter in our Universe.

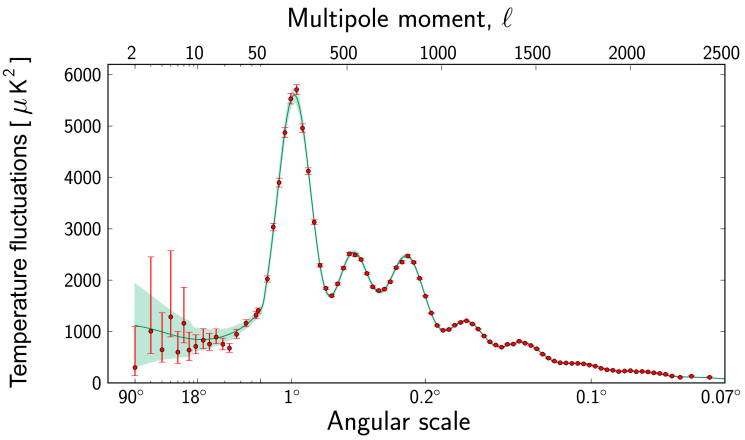

Figure 1: CMB power spectrum obtained from the Planck collaboration in 2013. The red dots are temperature measurements with corresponding error bars, and the green curve is the best parameter fit from a ΛCDM cosmological model. The second peak in the observed spectrum is the most famous one – it is namely a peak that disappears for all cosmological models containing $\Omega_b h^2 > 0.08$. Copyright: ESA and the Planck Collaboration [14].

2.2 Dark matter candidates

To summarise, it is put beyond reasonable doubt that our Universe contains dark matter, and that dark matter constitutes the majority of all existing matter. What we so far have learned about dark matter is a list of negative properties: it does not interact with electromagnetic radiation at any today observable wavelength, it can not be baryonic and it can not be relativistic, for structure formation reasons (among others). It is however stable, and it is affected by gravity. The evidence for dark matter resides to a great extent in the discrepancy between luminous matter and the matter derived from gravitational effects on other observables. One way to explain this discrepancy would be to say: there is something wrong with our understanding of gravity. This would be a fundamental turnover in physics, since not only Newtonian mechanics but also Einstein's general theory of relativity would need to be revised – but such turnovers have happened before.

Modified gravity models that account for dark matter range from Milgroms classical modification of Newtonian dynamics (MOND) to later theories based upon high energy corrections of the gravitational interaction or the scale invariance of empty space [15–17] . These models all have difficulties explaining the grand diversity of dark matter evidence, especially the CMB power spectrum and the structure formation. Furthermore, one of the strongest indications that modified gravity is not the answer to the dark matter question surprisingly comes from the *absence* of dark matter. In the past year, two galaxies that seem to lack dark matter have been found [18, 19]. This is extremely hard to explain

within the framework of modified gravity – if gravity is modified, it is not likely modified in separate ways from one galaxy to another.

This reinforces the use of "dark matter" as "unknown substance". What kind of substance is dark matter then? During the last century, fundamental physics has entered a particle paradigm – the Standard Model consists of 17 distinct particles and the Standard Model extensions are swamped with new, yet unconfirmed ones. The electromagnetic neutrality in combination with the non-relativistic and non-baryonic properties of dark matter rule out all of the Standard Model particles – neutrinos were for a long time considered as possible candidates, but this theory has been refuted due to upper bounds on the relic neutrino density (among other reasons) [7]. The research eye has since then turned to Standard Model extension particle models, of which a few is presented below. The models are split into two major categories depending on mass range: weakly interacting massive particles and light dark matter, the latter of which is the focus of this thesis.

2.2.1 Weakly interacting massive particles

The leading paradigm in astroparticle physics the past decades goes under the name WIMPs: Weakly Interacting Massive Particles. This is a theoretical framework describing electrically neutral particles in the mass range 1 GeV – 100 TeV, with interaction strengths up around the weak nuclear force scale. Such particles could have been produced in the early Universe through their chemical decoupling from the thermal bath. WIMP is rather a category of dark matter models than a specific type of particle – examples of particles contained within the WIMP collection are light neutralinos, the superpartners of the neutral Gauge and Higgs Standard Model bosons in supersymmetry (supersymmetry will be explained further in the context of light dark matter); particles coming from an extended Higgs sector; or Kaluza-Klein states, massive particle states stemming from vibration modes in fields living in dimensions beyond our space time [20, 21].

The experimental search for WIMPs has been remarkable in the past decade [20]. Three complementary procedures have been used:

- *Direct detection experiments*, where signals of Milky Way WIMPs scattering off detector target nuclei are traced in deep underground detectors with low background noise.
- *Indirect detection experiments*, where products of WIMP annihilation or decay in the Milky Way are searched for with satellites and ground based telescopes.
- *Particle collider experiments*, where missing energy in high energy collision spectra of known particles are analysed in search for WIMPs produced in the process.

Despite the major research investment in this area, WIMPs have so far escaped non-ambiguous detection. There is however one experimental collaboration that for the past two decades claims to

have found dark matter in the WIMP mass range: the DAMA/LIBRA collaboration [22]. They use direct detection and the claimed discovery is based on annual modulation signals, that measures the modulation of the scattering events over time. Since the detector direction relative the Milky Way dark matter halo changes with the rotation of the Earth around the sun, such an annual modulation is expected: when Earth is aligned with the halo, the signal should be stronger, and vice versa. Unfortunately, no other experiment has been able to reproduce the DAMA result, although efforts to mimic their exact experimental setup are currently made [20, 23]. Hence it is not considered to be a discovery.

All other experiments are instead constantly producing negative search results. For particle candidates in the mass range 10 GeV–10 TeV, direct detection experiments such as the XENON1T collaboration have limited the scattering cross sections to very small levels, without detecting any dark matter induced nuclear recoils [24, 25]. Nor have indirect detection experiments lead to a discovery of a dark matter particle within the WIMP framework. Another strong indication against the WIMP paradigm is the absence of non-Standard Model physics at particle colliders, such as the Large Hadron Collider (LHC) at CERN – this also narrows down the window for a potential WIMP discovery [26]. The theoretical motivation for WIMPs is hence lessened by this.

2.2.2 Light dark matter

One alternative to the WIMP theory that has gained a lot of interest over the past years is Light Dark Matter (LDM), a dark matter model category describing particles in the keV–GeV mass range. This is lighter than the WIMPs, but still not light enough to be relativistic and therefore part of the unlikely hot dark matter scenario. There is a wide variety of models for LDM, explaining the relic abundance needed to match the current amount of dark matter in the Universe, as well as the possible interactions with Standard Model particles.

Some of them are incorporated in the supersymmetric framework that has swept the physics world off its feet in the past decades, for example gravitinos [27] and axinos [28]. Supersymmetry is an extension of the Standard Model, presenting supersymmetric partners of all known (and unknown) particles. The partnership is based on spin – for each fermion the superpartner is a boson and vice versa, and these are created in pairs. Supersymmetry was introduced to solve other problems than the dark matter question in fundamental physics, such as the hierarchy problem, but it has since then been applied in a wide area of new physics. The lightest supersymmetric particle should be stable, since it can not decay to any lighter particle couples, and if it is neutral as well it is a candidate for dark matter. In order to establish a reasonable dark matter relic density, all the neutral Standard Model particles would have supersymmetric partners beyond the LDM mass range; neutralinos are in the WIMP range and sneutrinos (partners of neutrinos) even higher [7]. Hence only the wild cards are left: the gravitino, partner of the yet unseen graviton; and the axino, partner of the tiny axion

postulated to solve the CP problem but not discovered.

Other models imply a dark sector similar to the visible Standard Model sector, where the dark matter particles can be composite states – in analogy with mesons or hadrons – and the present-day abundance originates from an asymmetry between particles and antiparticles [29]. This theory goes under the name asymmetric dark matter. Another proposition is so called sterile neutrinos: new right-handed sisters to the left-handed Standard Model neutrinos [30]. Sterile neutrinos do not exhibit weak interactions, but they do interact with the Standard Model neutrinos, through oscillations between left- and right-handed particle states.

There is a wide variety of alternatives concerning how, and to what extent, the particles in this hypothetical dark matter zoo interact with the Standard Model particles. They could couple directly to Standard Model particles, interactions could be induced from higher-dimensional operators at loop level, or they could be enabled by an invisible mediator; an axion, a dark photon or an electromagnetic dipole moment, etc. LDM should however in theory be possible to detect. Since LDM in many ways is just a lighter variant of a WIMP, detection techniques similar to the ones used for the WIMP search can also be used for the LDM search. This is the main reason why the experimental search for LDM has gained a lot of interest over the last years. LDM is a broad theoretical framework still unconstrained by the exclusion limits weighing down the WIMP paradigm, but with large detection possibilities.

2.3 Experimental searches for light dark matter

As described in the WIMP scenario, there are three different experimental setups aiming to detect dark matter: direct detection, indirect detection, and production of dark matter in particle accelerators. All of these procedures can be used in the search for LDM, with slight modifications compared to the WIMP search, which most of the experiments existing today were initially built for. The focus in this thesis is direct detection of LDM, thus this will be described in more detailed than the other two detection techniques.

2.3.1 Indirect detection

Indirect detection searches for Standard Model particles produced by dark matter processes in space. One such process is annihilation – which of course requires dark matter antiparticles to exist and to be abundant enough to generate a detectable signal. The other is decay, which also could give rise to Standard Model particle production, provided that dark matter has a limited lifetime. Different experimental setups are needed for detection of different final products: neutrinos, gamma rays, cosmic rays, etc. The main drawback with this approach is that it is difficult to distinguish dark matter processes from all other astrophysical processes constantly occurring in space.

In the framework of LDM, there are a few recent developments and suggestions to solve the background issue. For example, if dark matter couples primarily to quarks, the annihilation or decay of

Milky Way dark matter particles could generate detectable photon signals [31]. These signals would stand out in a spectrum since there are quite few particles that can be generated from a process with centre-of-mass energy in the sub-GeV range. One of the possible particle candidates is the η-meson, so annihilating or decaying dark matter in the above theoretical framework have the potential to produce specific photon spectra through η-mesons decaying to photons.

Other possible dark matter particle physics frameworks suitable for indirect detection of LDM are studied in [32], where the gravitino and the sterile neutrino, among others, are explored. The experimental setup considered there is diffuse X-ray and gamma ray observations, originally measured in the WIMP search but reinterpreted in the LDM framework.

2.3.2 Particle colliders

The search for dark matter in particle colliders is a search for missing energy due to production of undetectable dark matter particles. These dark matter particles can, as a kind of reversed indirect detection process, be produced either in Standard Model particle decays or in a particle-antiparticle creation. The processes where LDM can be created have lower centre-of-mass energy compared to the WIMP scenario, so the high-energy colliders such as LHC are not relevant in the LDM search. Instead, low energy electron and positron collisions are analysed. BaBar and BELLE(II) are the leading facilities for such collisions, and the results from these particle colliders have been analysed in the LDM framework [33, 34].

Production of dark matter through B-meson decays in low energy collisions were initially considered to be a promising channel of probing LDM [35]. These meson decays are though very rare, so other possibilities have been explored too. If the dark matter production is mediated through for example a dark photon, it could give rise to a larger missing energy in electron-positron collisions [36].

One overall challenge in the search of dark matter in particle colliders is that neutrinos also display themselves as missing energy in the spectra, so the division between the two is hard. Furthermore, even if a new particle were to be found in these experiments, it would still not be certain that this new discovery was dark matter – there are plenty of other new particle candidates that does not necessarily constitute 85% of the matter content in the Universe.

2.3.3 Direct detection

Direct detection experiments are based on the scattering of Milky Way dark matter particles and Earth-based detector targets. Provided that dark matter interacts, directly or via a mediator of some kind, with Standard Model particles, such scattering events would in principal be possible to detect on Earth. Since these interactions are expected to be quite weak – after all, no interactions of dark matter have yet been detected – a crucial part of the experiment is the background noise. For this reason, direct detection experiments are often placed deep underground [37]. This shields the detector from

uninvited space travelling particle guests, for example cosmic muons. Muons produced when cosmic rays meet the upper atmosphere can travel all the way down to a ground based detector without decaying or annihilating, thus creating a misleading signal. Luckily, they can not as easily pass the crust of the Earth. Other background sources are external neutrons, electrons induced by gamma radiation in the surrounding bedrock, or internal detector radiation.

Today a great range of different detection target and experimental procedures exists: superheated fluids, liquid noble gases, scintillators, crystal semiconductors, etc [37]. These were all initially designed to capture WIMPs, thus measuring the nuclear recoil induced by WIMP scattering. However, in a 2012 paper by Essig, Mardon and Volansky [2], it was proposed that some of these experimental setups could also be used in the search for LDM in the mass range MeV–GeV. This is possible if one measures the *electron recoil* instead of the nuclear recoil, which for the LDM mass range is beyond the reach of current experimental thresholds.

The possibility to detect a signal in a WIMP direct detection experiment is determined by the energy of the recoiling nucleus E_{NR}, and thus the transferred momentum q since $E_{NR} = q^2/2m_N$. The maximum value of q occurs when the angle between the incoming dark matter velocity v and the nuclear recoil is 0. Through energy and momentum conservation, this is determined to $q_{\max} = 2\mu_{N,\chi}v$, where $\mu_{N,\chi}$ is the reduced mass of the nucleus and the dark matter particle [38]. If we assume that $m_\chi \ll m_N$ and approximate the dark matter velocity to $10^{-3}c$, this yields an upper limit for the recoil energy E_{NR} [39]:

$$E_{NR} = \frac{q^2}{2m_N} \leq \frac{2\mu_{N,\chi}^2 v^2}{m_N} \simeq 1\,\text{eV} \times \left(\frac{m_\chi}{100\,\text{MeV}}\right)^2 \left(\frac{20\,\text{GeV}}{m_N}\right). \tag{2.7}$$

Here, the numbers have been rearranged to prefixes, to create a simple overview. For a dark matter mass of a few hundreds of MeV, the nuclear recoil energies are a few tens of eV. When comparing this result to the current thresholds for detecting these signals in experimental setups, which often are of order keV [25], the case for looking at dark matter-electron scattering instead is clearly made. Since the electron is much lighter than the nucleon and the dark matter-electron scattering is naturally inelastic, the dark matter particle can transfer a large fraction of its kinetic energy to the electron, causing a detectable ionization signal even for ~ 1 MeV dark matter masses [39].

Unfortunately, bound electrons are a bit trickier to handle than nuclei. For example, bound electrons have indefinite momentum, which complicates the kinematics involved in the process – the momentum transfer is no longer directly linked to the deposited energy as in the case of nuclear scattering. The signal rate is also highly dependant on the electron structure in the detector material, which especially in the case of semiconductor targets can be quite complicated [39]. This complex electron behaviour can however be encoded in an atomic form factor, which is independent of the dark matter model used. In addition to this atomic form factor, the observable direct detection signal rate depends on the velocity distribution of the dark matter particles in the Milky Way halo and the dark

matter particle model; the dark matter mass and the underlying interaction theory for the relevant particles.

The technique to detect small electron ionization and excitation signals in direct detection experiments is currently being explored for noble gas targets used by the DarkSide50-, XENON10- and LUX-collaborations [40–42], and for crystal semiconductor targets used by the SuperCDMS- and SENSEI-collaborations [43, 44]. In this thesis, three detector targets will be used: argon, xenon and germanium. The goal of the analysis of dark matter-electron scattering rates is to distinguish between dark matter that is its own antiparticle and dark matter that has a separate antiparticle – a feature that could help us understand what dark matter really is.

2.4 Particle/antiparticle nature

What is an antiparticle? An easy visualisation that is common in upper secondary schools is the one with the paper and the scissors. A white paper represents energy, then a circle is cut out from the paper to represent the particle. The antiparticle is now the hole in the paper – similar to the circle in size but different in substance, defined as an absence rather than an existence. When the circle is reinstated in its original place, the white paper is whole again: the particles have annihilated to energy. This is of course an oversimplification, but the idea that antiparticles are "holes" were actually first proposed by Paul Dirac when he stumbled across the negative energy solutions to his equations that were to be called antiparticles [45]. This metaphor was however made obsolete by quantum field theory (QFT), which explains antiparticles as negative energy states of the ordinary particle field. Since positive energy states correspond to particles moving forward in time, the QFT visualisation of antiparticles is particles moving backwards in time. How to explain that with a paper and a pair of scissors is though beyond my imagination.

To be more physical: an antiparticle shares all properties with its particle, except for the fact that all quantum charges are reversed. It has the opposite electromagnetic charge, the opposite baryon/lepton number, the opposite colour charge, etc. A particle that is its own antiparticle must therefore be fundamentally neutral. The neutron is for example not fundamentally neutral, it consists of quarks with colour charges, and hence has an antiparticle which consists of the corresponding antiquarks. The photon is on the contrary its own antiparticle: it has no charges whatsoever. There are no known fermions that are their own antiparticles – although the particle/antiparticle nature of neutrinos are yet debated and currently probed in experiments [46]. A fermion that is its own antiparticle is a Majorana particle, named after Ettore Majorana and postulated as an alternative to the traditional Dirac fermion, to explain the nature of the neutrino.

Dark matter, just like the neutrino, is a particle candidate that could be its own antiparticle – the electromagnetic neutrality and the lack of interactions are the only fairly established facts we have regarding the nature of dark matter. In 2016, a test to determine whether dark matter is different

from its antiparticle was proposed by Queiroz, Rodejohann and Yaguna [4]. The proposition was to combine the results of three different direct detection experiments, in order to separate the theoretical predictions for the expected signal rate generated by a Dirac or a Majorana fermion. The reasoning can however be generalised to scalar or vector dark matter too.

The test is based on spin independent, general interactions between dark matter and nuclei. Hence the dark matter model considered is the WIMP scenario. The direct detection data is interpreted in the Majorana framework, and after comparing the rates of three different detector targets an inconsistency in this interpretation can be established. It is therefore possible to reject the possibility that dark matter is its own antiparticle, but not to prove this to be true. A crucial part of the discrimination procedure is the fact that dark matter has distinct couplings to on the one hand the neutrons and on the other hand the protons of the detector target. If dark matter would couple only to protons or only to neutrons, discrimination would be impossible.

In this thesis, the test proposed by Queiroz, Rodejohann and Yaguna will be applied within a light dark matter framework instead, where dark matter scatter of electrons instead of nuclei in direct detection experiments. In the next chapter, the mathematical framework of dark matter-electron scattering and the corresponding observable in direct detection experiments based on liquid noble gases and semiconductors will be presented, as well as the underlying quantum field theory behind the particle/antiparticle nature of dark matter.

3 Theoretical framework

The mathematical framework of this project is divided in two distinct parts: dark matter models, and the scattering process in direct detection. The first part contains the particle physics theory behind the relevant dark matter models. Assuming spin $\frac{1}{2}$-dark matter particles, the mathematical representation of these are spinor fields. The particle/antiparticle nature is determined by how these fields transform under charge conjugation: a Dirac particle is turned into its antiparticle under charge conjugation, whereas a Majorana particle remains the same. This difference leads to a distinction in interaction cross sections in free space. The cross sections are linked to the scattering event rates, that are explored in the second part of this section. These are the actual observables that can be measured in direct detection experiments.

All equations from here on are expressed in natural units, that is, $\hbar = c = 1$.

3.1 Dark matter models

Two dark matter models are explored in this section: one where the dark matter field couples directly to electrons, and one where the dark matter-electron interaction is mediated by a photon. It is shown that the former leads to Dirac and Majorana cross sections that are impossible to experimentally distinguish from one another, thus the latter is used throughout the project. However, let us begin with the theory of spinor fields and charge conjugation – the transformation that turns a particle into its antiparticle.

3.1.1 Dirac fields and charge conjugation

Antiparticles were discovered as naturally arising negative energy solutions to one of the most famous equations in theoretical physics: the Dirac equation. The Dirac equation is an equation of motion for free fermions, represented by spinor fields ψ. The following presentation of such spinors and their properties is based on [47]. A spinor is characterised by its typical transformation under a Lorentz boost or rotation, and the Dirac equation is originally a classical field equation that manifestly inherits relativistic invariance. It follows through variation of the action of the Dirac Lagrangian:

$$\mathcal{L}_{\text{Dirac}} = \bar{\psi}(i\gamma^\mu \partial_\mu - m)\psi \quad \Rightarrow \tag{3.1}$$

$$0 = (i\gamma^\mu \partial_\mu - m)\psi. \tag{3.2}$$

Here, $\bar{\psi} = \psi^\dagger \gamma^0$ and the γ-matrices fulfill the Dirac algebra

$$\{\gamma^\mu, \gamma^\nu\} = 2g^{\mu\nu}. \tag{3.3}$$

One explicit realisation of this algebra is the Weyl, or chiral, representation

$$\gamma^0 = \begin{bmatrix} 0 & 1 \\ 1 & 0 \end{bmatrix}; \quad \gamma^i = \begin{bmatrix} 0 & \sigma^i \\ -\sigma^i & 0 \end{bmatrix}, \tag{3.4}$$

where σ^i are the Pauli matrices. The free particle solutions of the Dirac equation (3.2) is naturally split up into two distinct parts:

$$\psi(\vec{x}) = \begin{cases} u^s(\vec{p})e^{-i\vec{p}\cdot\vec{x}} & \Leftrightarrow \quad \text{positive energy solutions,} \\ v^s(\vec{p})e^{+i\vec{p}\cdot\vec{x}} & \Leftrightarrow \quad \text{negative energy solutions.} \end{cases} \tag{3.5}$$

In the above notation, s is a spin index and $\vec{p}$ is the particle momentum. This is the distinction between particles and antiparticles that arises in the Dirac equation: the positive energy solutions labelled by the spinor u^s correspond to the particles; the negative energy solutions labelled by the spinor v^s correspond to antiparticles.

The quantization of the Dirac field is done by imposing the canonical anticommutation relations

$$\{\psi_a(\vec{x}), \psi_b^\dagger(\vec{y})\} = \delta^{(3)}(\vec{x} - \vec{y})\delta_{ab}; \tag{3.6}$$

$$\{\psi_a^\dagger(\vec{x}), \psi_b^\dagger(\vec{y})\} = \{\psi_a(\vec{x}), \psi_b(\vec{y})\} = 0. \tag{3.7}$$

These relations are necessary in order to ensure that the vacuum has only positive-energy excitations, and they also entail that two identical fermions can not fill the same state, i.e that they obey the Pauli exclusion principle. The anticommutation relations are fulfilled through the introduction of creation and annihilation operators $a_{\vec{p}}, a_{\vec{p}}^\dagger, b_{\vec{p}}, b_{\vec{p}}^\dagger$, where the a:s act on particles and the b:s on antiparticles. These operators obey the relations

$$\{a_{\vec{p}}^r, a_{\vec{q}}^{s\dagger}\} = \{b_{\vec{p}}^r, b_{\vec{q}}^{s\dagger}\} = (2\pi)^3\delta^{(3)}(\vec{p} - \vec{q})\delta^{rs}, \tag{3.8}$$

where r, s are spin indices and $\vec{p}, \vec{q}$ are momentum. The quantized Dirac field is in this notation

$$\psi(\vec{x}) = \int \frac{d^3p}{(2\pi)^3} \frac{1}{\sqrt{2E_p}} \sum_s \left(a_{\vec{p}}^s u^s(\vec{p}) e^{-i\vec{p}\cdot\vec{x}} + b_{\vec{p}}^{s\dagger} v^s(\vec{p}) e^{i\vec{p}\cdot\vec{x}} \right); \tag{3.9}$$

$$\bar{\psi}(\vec{x}) = \int \frac{d^3p}{(2\pi)^3} \frac{1}{\sqrt{2E_p}} \sum_s \left(b_{\vec{p}}^s \bar{v}^s(\vec{p}) e^{-i\vec{p}\cdot\vec{x}} + a_{\vec{p}}^{s\dagger} \bar{u}^s(\vec{p}) e^{i\vec{p}\cdot\vec{x}} \right). \tag{3.10}$$

Out of these spinor fields ψ and $\bar{\psi}$, five bilinears with definite transformation properties under the

Lorentz group can be formed:

$$\bar{\psi}\psi, \qquad \bar{\psi}\gamma^{\mu}\psi, \qquad \bar{\psi}\gamma^{\mu}\gamma^{5}\psi, \qquad i\bar{\psi}\gamma^{5}\psi, \qquad \bar{\psi}\sigma^{\mu\nu}\psi, \tag{3.11}$$

where $\gamma^5 = i\gamma^0\gamma^1\gamma^2\gamma^3$ and $\sigma^{\mu\nu} = i/2[\gamma^{\mu}, \gamma^{\nu}]$. Hence, only these five bilinears are allowed in a Lorentz invariant Lagrangian. It is therefore the behaviour of these terms under charge conjugation that will determine the possible Lagrangians for Dirac fields and Majorana fields. The crucial difference between the two is that Majorana fields can only have terms that are *even* under charge conjugation in the system Lagrangian, whereas Dirac fields can also have *odd* terms.

Charge conjugation C preserves spin orientation but reverses all charges of the particle, thus turning it into its antiparticle:

$$Ca^{s}_{\vec{p}}C = b^{s}_{\vec{p}}, \quad Cb^{s}_{\vec{p}}C = a^{s}_{\vec{p}}. \tag{3.12}$$

By applying the operator C on the Dirac fields in equations (3.9) and (3.10), the behaviour of the five bilinears (3.11) under charge conjugation can be determined. In table 1 the result of this is shown [47]. Here the derivative operator ∂_μ has also been included.

Table 1: Table over charge conjugation properties of the Dirac field bilinears.

	$\bar{\psi}\psi$	$i\bar{\psi}\gamma^5\psi$	$\bar{\psi}\gamma^{\mu}\psi$	$\bar{\psi}\gamma^{\mu}\gamma^5\psi$	$\bar{\psi}\sigma^{\mu\nu}\psi$	∂_μ
C	even	even	odd	even	odd	even

3.1.2 Dark matter-electron interactions

At leading order in the non-relativistic limit, the most general Lagrangian describing interactions between fermionic dark matter and electrons in free space, when only the spin-independent parts are considered, is

$$\mathcal{L}_{SI} = C_e\bar{\psi}_{\chi}\psi_{\chi}\bar{\psi}_e\psi_e + C_o\bar{\psi}_{\chi}\gamma_{\mu}\psi_{\chi}\bar{\psi}_e\gamma^{\mu}\psi_e, \tag{3.13}$$

where C_e and C_o are couplings of dimension [energy^{-2}], ψ_e is the electron field and ψ_χ is the dark matter field. This Lagrangian is the electron analogy to the dark matter-nucleon interaction Lagrangian presented by Queiroz, Rodejohann and Yaguna, in the 2016 paper that proposes the method to determine the dark matter particle/antiparticle nature used in this thesis [4]. Since the cross section for any interaction is dominated by the spin-independent contributions, this is a reasonable starting point. The Lagrangian is split up in two terms: on the one hand, the part which is even under charge conjugation, depending on C_e, on the other hand, the part which is odd under charge conjugation, depending on C_o. The division is made from the properties of the Dirac bilinears, showed in table 1.

For Majorana fields, C_o must be equal to zero, and for Dirac fields both terms can be present.

In a direct detection experiment, the number of detected signal events will depend on the free interaction cross section between the scattering particles. This cross section, describing the area perpendicular to the relative particle motion, within which the particles must meet in order to scatter, is calculated from the Lagrangian [47]. Following [4] but with electron fields instead of nuclei fields, the cross section for the Majorana case is

$$\sigma_{SI}^{M} = \frac{4\mu_{\chi,e}^2}{\pi} C_e^2, \tag{3.14}$$

where $\mu_{\chi,e}$ is the reduced mass of the electron and the dark matter particle. For Dirac fields, particles would have the same cross section as in the Majorana case but with C_e replaced with $C_D = 1/2(C_e + C_o)$, and antiparticles would have C_e replaced with $C_{\bar{D}} = 1/2(C_e - C_o)$. Under the assumption that particles and antiparticles contribute equally to the cross section, this yields the total cross section

$$\sigma_{SI}^{D} = \frac{4\mu_{\chi,e}^2}{\pi}\frac{1}{2}(C_D^2 + C_{\bar{D}}^2) = \frac{2\mu_{\chi,e}^2}{\pi}\frac{1}{4}(2C_e^2 + 2C_o^2) \Rightarrow \tag{3.15}$$

$$\sigma_{SI}^{D} = \frac{\mu_{\chi,e}^2}{\pi}(C_e^2 + C_o^2). \tag{3.16}$$

When comparing the Dirac and Majorana cross sections in equations (3.14) and (3.16), one sees that they only differ in their coefficients. In fact, the Dirac cross section can be mapped to the Majorana cross section through the transformation

$$C_o^2 \to 3C_e^2, \quad \Rightarrow \quad \sigma_{SI}^{D} \to \sigma_{SI}^{M}. \tag{3.17}$$

The couplings C_e and C_o are not measurable in themselves, they can only be derived from the application of a theoretical particle physics framework to the number of detected scattering events in an experiment. In such a framework, it will be impossible to separate the scenario where the data comes from a single Majorana coupling C_e from the one where it comes from the Dirac combination of C_e and C_o. For an infinite number of (C_e, C_o)-pairs, the Dirac and Majorana cross section are indistinguishable.

Hence the conclusion: in a direct detection experiment founded on a theoretical framework governed by the Lagrangian in equation (3.13), it is impossible to tell whether the dark matter particle has a distinct antiparticle or not.

3.1.3 Dark matter-photon interactions

In order to discriminate the Dirac from the Majorana cross sections, one has to look into another particle physics scenario. The problem with the Lagrangian in equation (3.13) is that the electron field couples to the dark matter Majorana and Dirac field in a similar way. This problem was already noticed by [4] in the context of dark matter-nucleus scattering; discrimination between Dirac and Majorana is only possible if dark matter couples to *both* protons and neutrons (as described in section 2.4). The problem will therefore persist even in a spin-dependent extension of the theory. To avoid this, a theoretical framework where the interaction is mediated by another particle can be used.

Kavanaugh, Panci and Ziegler have explored the possible interactions between dark matter particles and photons in a 2018 paper [3]. Even though dark matter is dark, in the sense that it does not absorb or emit detectable light, it can still interact with photons. If this interaction is to occur at tree level, that is when all particle momenta are determined by conservation laws, dark matter needs to have an electric charge. There are dark matter models which include such a charge, called "milli-charge" to emphasise the small size of this compared to the electron charge [48, 49]. The neutrality condition for dark matter is hence softened to a neutrality facade: the dark matter electric charge is in practice zero, since it is too small to be detected. However, an electric charge excludes the possibility for dark matter to be a Majorana fermion, which is why the millicharged theories are not considered here. The dark matter-photon interactions thus occur at loop level instead of tree level.

Loop level interactions are interactions involving virtual particles with momenta that are not determined by conservation of momentum, hence these uncertain momenta must be integrated over in the perturbation theory calculations. Loop level dark matter-photon interactions arise from operators of energy dimension five or higher. For fermionic dark matter, the loop level dark matter-photon Lagrangian in free space for the Majorana and the Dirac case, given in [3], is

$$\mathcal{L}_\gamma^M = \frac{e}{16\pi^2}\left(\frac{C_1}{2}\bar{\psi}\gamma^5\psi\cdot\partial^\nu F_{\mu\nu}\right); \tag{3.18}$$

$$\mathcal{L}_\gamma^D = \frac{e}{16\pi^2}\left(\frac{C_1}{2}\bar{\psi}\gamma^5\psi\cdot\partial^\nu F_{\mu\nu} + \frac{C_2}{2}\bar{\psi}\sigma^{\mu\nu}\psi\cdot F_{\mu\nu} + \frac{C_3}{2}i\bar{\psi}\sigma^{\mu\nu}\gamma^5\psi\cdot F_{\mu\nu}\right). \tag{3.19}$$

Here C_1, C_2, C_3 are the coupling coefficients, which have dimension $[\text{energy}]^{-2}$, $[\text{energy}]^{-1}$, $[\text{energy}]^{-1}$ respectively, e is the electron charge and $F_{\mu\nu}$ is the electromagnetic Maxwell field. There are additional terms, but since they are of higher order in energy they have been cut off; only the leading order energy terms in each scenario are kept.

To get the connection to the electron field ψ_e, we can rewrite $\partial^\nu F_{\mu\nu}$ in terms of currents of electrons, using the equation of motion in quantum electrodynamics;

$$\partial^\nu F_{\mu\nu} = e\bar{\psi}_e \gamma^\mu \psi_e. \tag{3.20}$$

Now the matrix elements can be derived for the two Lagrangians in equations (3.18) and (3.19). The squares of these matrix elements are proportional to the scattering cross sections, encoding the theoretical framework of free interaction between the dark matter and the Standard Model particle.

These matrix elements are calculated for each term in the Lagrangians by summing over the relevant quantum mechanical operators, encoding different couplings between the dark matter spin and the electron spin. The operators are different scalar combinations of the spin vectors, the momentum $\vec{q}$ transferred from the dark matter particle to the electron, and the transverse dark matter-electron velocity $\vec{v}^{\perp}$. The transverse velocity is

$$\vec{v}^{\perp} = \vec{v} - \frac{\vec{q}}{2\mu_{\chi,e}} - \frac{\vec{k}}{2m_e}, \tag{3.21}$$

where $\vec{k}$ is the momentum of the incoming electron. In the calculation, the last term in the above expression was however discarded. If it were to be present, the matrix elements would need to be included in the integral over electron momentum in the scattering rate of a bound electron, which would complicate things a lot. Therefore, the simplification $\vec{v}^{\perp} \approx \vec{v} - \vec{q}/(2\mu_{\chi,e})$ was made.

The squared matrix elements that describe the interaction between a dark matter particle and an electron, through loop level photon mediation, are given below for the Dirac and the Majorana scenario. They are averaged over initial spins and summed over final spin states. In these expressions, the electron Landé factor g_e and the fine structure constant α appear.

$$\overline{|\mathcal{M}^M_{\text{free}}|^2} = C_1^2 8\pi\alpha \left(q^2 g_e^2 m_\chi^2 + 8 m_\chi^2 m_e^2 v^2 - 2q^2(m_\chi + m_e)^2\right) \tag{3.22}$$

$$\overline{|\mathcal{M}^D_{\text{free}}|^2} = \overline{|\mathcal{M}^M_{\text{free}}|^2} + 32\pi\alpha m_\chi \left[C_2^2 \left(\frac{8 m_\chi m_e^2 v^2}{q^2} - 2(m_\chi + 2m_e) + g_e^2 m_\chi\right) + C_3^2 \frac{8 m_\chi m_e^2}{q^2}\right]. \tag{3.23}$$

The crucial difference between the above expressions is not anymore one of mere scaling, but of dependence on the momentum q, transferred from the dark matter particle to the electron, and dark matter velocity v. That is,

$$\begin{aligned} \overline{|\mathcal{M}^M_{\text{free}}|^2} &= C_1^2 \overline{|\mathcal{M}_1(q,v)|^2}, \\ \overline{|\mathcal{M}^D_{\text{free}}|^2} &= C_1^2 \overline{|\mathcal{M}_1(q,v)|^2} + C_2^2 \overline{|\mathcal{M}_2(q,v)|^2} + C_3^2 \overline{|\mathcal{M}_3(q,v)|^2}, \end{aligned} \tag{3.24}$$

where the terms in the equations (3.22) and (3.23) simply have been dubbed $\overline{|\mathcal{M}_1|^2}$ and $\overline{|\mathcal{M}_1|^2}$, $\overline{|\mathcal{M}_2|^2}$, $\overline{|\mathcal{M}_3|^2}$ respectively. This difference in q-dependence enables a discrimination between the Dirac and the Ma-

jorana nature. The two direct detection event rates will depend on q in different ways, hence one or the other can be a better fit to a set of experimental data. However, if C_2 and C_3 are zero, the Dirac particle model turns into the Majorana model. If the potential experimental signals are more compatible with the Majorana model, it is impossible to know whether dark matter actually is Majorana, or if it is Dirac with $C_2 = C_3 = 0$. This means that the Majorana nature of dark matter can never be proven in this theoretical framework, it can only be dismissed in favour of Dirac.

3.2 Dark matter-electron scattering in direct detection

Neither the coupling constants nor the matrix elements described in the previous section can actually be measured in an experiment. What is measurable in a direct detection experiment is the number of signal events, N, for a given exposure ξ = observation time $\times$ target mass and signal rate R. R is calculated from the differential scattering rate dR/dE for different detectable energies E, according to

$$N = \xi R = \xi \int \frac{dR}{dE} dE. \tag{3.25}$$

This differential scattering rate depends on the atomic structure of the target material, on the underlying dark matter particle model (encoded in the matrix element), and on astronomical properties of dark matter like the galactic velocity distribution and the density. The goal of this section is to derive expressions for these different parts of the scattering rate, for liquid noble gas targets as well as for crystal semiconductor targets. But first, an overview of the kinematics of dark matter-electron scattering, which motivates the overall use of direct detection experiments for LDM and sets up the guidelines for the scattering rate derivation.

3.2.1 Kinematics

The scattering process for a Milky Way dark matter particle hitting an electron in the detector target is shown in figure 2. Here, $\vec{p}$ is the incoming momentum of the dark matter particle, whereas $\vec{p}'$ is its outgoing momentum. The momentum lost by the dark matter particle during the scattering is denoted $\vec{q}$. In the case of nuclei scattering, the nucleus recoil energy would just be $E_{NR} = q^2/2m_N$. For dark matter-electron scattering however, this simple relation does no longer apply. This is due to the fact that the bound electron momentum is indefinite. Another difference from the nuclei case is that the energy deposited to the electron, E_d, is not only the electron recoil energy E_r, but also the binding energy E_b needed to excite the electron from the bound state:

$$E_d = E_b + E_r. \tag{3.26}$$

The energy of the incoming dark matter particle is however conserved and split up in the outgoing

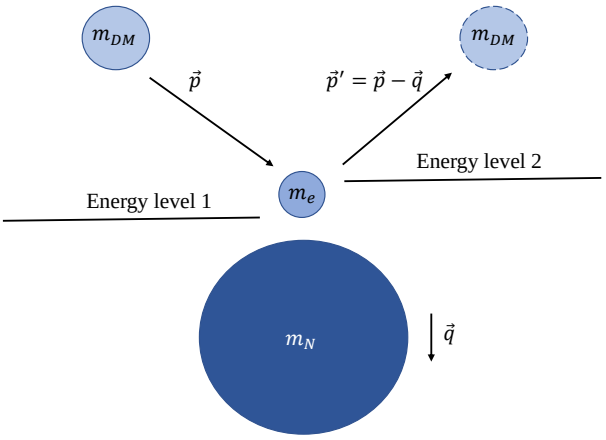

Figure 2: The scattering of a dark matter particle with a bound electron. The dark matter transfers momentum $\vec{q}$ to the target, resulting in a small nuclear recoil and a change in the electron energy. The electron is either excited to a higher energy level or to an ionized state. The vectors in the picture are scaled and directed in a non-conservative way, to show the scattering principle.

dark matter particle with momentum $\vec{p}' = \vec{p} - \vec{q}$, the nuclear recoil with momentum $\vec{q}$, and the energy deposited to the electron:

$$\frac{p^2}{2m_\chi} = \frac{|\vec{p} - \vec{q}|^2}{2m_\chi} + \frac{q^2}{2m_N} + E_d. \tag{3.27}$$

The nuclear recoil (second term on the RHS of equation (3.27)) is very small compared to the other terms and can therefore be neglected, which gives the following result:

$$E_d \simeq \frac{\vec{q} \cdot \vec{p}}{m_\chi} - \frac{q^2}{2m_\chi} = \vec{q} \cdot \vec{v} - \frac{q^2}{2m_\chi}, \tag{3.28}$$

where $\vec{v}$ as before is the velocity of the incoming dark matter particle. Setting $\vec{q} \cdot \vec{v} = qv$ yields the limit of the minimum dark matter velocity needed to deposit the energy E_d:

$$v_{\min} = \frac{E_d}{q} + \frac{q}{2m_\chi}. \tag{3.29}$$

From equation (3.28), one can also estimate the maximum energy that can be deposited to the electron, in order to see if dark matter particles in the LDM mass range can generate a signal in the

detectable energy interval. To find the largest possible E_d we need to maximize the energy with respect to q, besides setting $\vec{q}\cdot\vec{v} = qv$. This yields $q_{\max} = m_\chi v$, which for the typical dark matter velocity $v \sim 10^{-3}$ leads to

$$E_d \leq \frac{m_\chi v^2}{2} \simeq \frac{1}{2}\text{eV} \times \left(\frac{m_\chi}{\text{MeV}}\right). \tag{3.30}$$

This is clearly more promising than the nuclear recoil energy estimation given in equation (2.7), which was below experimental thresholds for dark matter masses below $\sim$ GeV. Germanium has a bandgap of order $\sim$eV, hence signals of this size can be detected [39]. That means dark matter particles with masses in the MeV-range are detectable. The limits for argon and xenon detectors are a bit higher, but for the outer shell electrons the binding energies are of order $\sim$ 10 eV, making masses down to 20 MeV detectable.

The above calculation is only an upper limit based on a specific q-value though. What about the average transferred momentum? The electron velocity is $v_e \sim Z_{\text{eff}}\alpha$, where Z_{eff} is the effective charge felt by the electron. For outer shell electrons, Z_{eff} is approximately 1 and $v_e \sim \alpha \sim 10^{-2}$. This is one order of magnitude higher than the typical dark matter velocity of 10^{-3}, and therefore the relative velocity between the two is dominated by v_e. The typical transferred momentum is therefore

$$q_{\text{typ}} \sim m_e v_e \sim Z_{\text{eff}}\alpha m_e \simeq Z_{\text{eff}} \times 4\,\text{keV}. \tag{3.31}$$

Since Z_{eff} is of order 1, q_{typ} is of order keV.

To estimate what kind of energies are typically deposited to the electron, one can consider the minimum momentum transfer q required to deposit an energy E_d. For low q, E_d in equation (3.28) is dominated by the term $\vec{q}\cdot\vec{v}$. The momentum transfer is then limited by

$$q \geq \frac{E_d}{v}. \tag{3.32}$$

Hence, the typical momentum transfer will deposit an energy $E_d \sim v q_{\text{typ}} \sim 10^{-3}\,\text{keV}$, meaning that the typical deposited energies are of order eV. In order to excite or ionize a bound electron, the deposited energy must be greater than the binding energy. This leads to the conclusion that mostly outer shell electrons can cause a detectable signal. The inner shell electrons have binding energies higher than the typical deposited energies, and will therefore contribute only little to the event rate.

To sum up: for dark matter-electron scattering, the energy deposited to the electron depend both on the transferred momentum and on the dark matter velocity, and this energy needs to be greater than the binding energy of the initial electron for a signal to occur. These facts will direct the computation of the scattering event rates.

3.2.2 Scattering cross section

The scattering rates in direct detection depend on the cross section $\sigma_{1\to2}$ for an electron transition from energy level 1 to 2, induced by a dark matter particle. This rate $R_{1\to2}$ is given by

$$R_{1\to2} = \frac{\rho_\chi}{m_\chi} \int d^3v g_\chi(\vec{v}) \sigma_{1\to2} v_{\text{rel}}, \tag{3.33}$$

where v_{rel} is the relative velocity between the dark matter particle and the electron, $g_\chi(\vec{v})$ is the velocity distribution of dark matter in the Milky Way halo, and ρ_χ is the dark matter density. The scattering cross section $\sigma_{1\to2}$ is derived from the free scattering cross section σ_{free} of χ $(\vec{p})$ + e^- $(\vec{k})$ $\to$ χ $(\vec{p}\,')$ + e^- $(\vec{k}\,')$, which is a standard quantum field theory computation. A transformation from this to the bound electron case is then made. Dark matter is considered non-relativistic throughout this process.

The cross section for free scattering, given for example in [47], is

$$\sigma_{\text{free}} = \frac{1}{v_{\text{rel}}} \int \frac{d^3q}{(2\pi)^3} \frac{d^3k'}{(2\pi)^3} \frac{1}{16 E'_\chi E_\chi E'_e E_e} (2\pi)^4 \delta(E_i - Ef) \delta^3(\vec{p} + \vec{k} - \vec{k}\,' - \vec{p}\,') \overline{|\mathcal{M}_{\text{free}}(q,v)|^2}, \tag{3.34}$$

where E_e and E'_e are the initial and final electron energy, E_χ and E'_χ are the initial and final dark matter energy, E_i and E_f are the total initial and final energies and $\mathcal{M}_{\text{free}}$ is the matrix element from the previous section, which is a function of transferred momentum q and dark matter velocity v. Momentum conservation requires $\vec{q} = \vec{p} - \vec{p}\,' = \vec{k}\,' - \vec{k}$. The non-relativistic scattering amplitude for this process is

$$\langle \chi_{\vec{p}\,'}, e_{\vec{k}\,'} | H_{\text{int}} | \chi_{\vec{p}}, e_{\vec{k}} \rangle = C \mathcal{M}_{\text{free}}(q,v) (2\pi)^3 \delta^3(\vec{p} + \vec{k} - \vec{k}\,' - \vec{p}\,'). \tag{3.35}$$

Here H_{int} is the interaction Hamiltonian, C is a constant and $|\chi_{\vec{p}}, e_{\vec{k}}\rangle$ are plane-wave states.

If the electron is bound to an atom instead of being free, the electron momenta $\vec{k}$ and $\vec{k}\,'$ are indefinite, and an integration over the phase space needs to be performed. The scattering amplitude of the electron transition from state 1 to state 2 turns into

$$\langle \chi_{\vec{p}\,'}, e_2 | H_{\text{int}} | \chi_{\vec{p}}, e_1 \rangle = \left[\int \frac{\sqrt{V} d^3k'}{(2\pi)^3} \tilde{\psi}_2^*(\vec{k}\,') \langle \chi_{\vec{p}\,'}, e_{\vec{k}\,'} | \right] H_{\text{int}} \left[\int \frac{\sqrt{V} d^3k}{(2\pi)^3} \tilde{\psi}_1(\vec{k}) | \chi_{\vec{p}}, e_{\vec{k}} \rangle \right], \tag{3.36}$$

where $\tilde{\psi}_1$ and $\tilde{\psi}_2$ are unit normalized wave functions in momentum-space for the initial and final electron, and V is the space normalization volume. Expanding this expression yields

$$\langle \chi_{\vec{p}\,'}, e_2|H_{\rm int}|\chi_{\vec{p}}, e_1\rangle = V\int\int \frac{d^3k'd^3k}{(2\pi)^6}\tilde{\psi}_2^*(\vec{k}\,')\tilde{\psi}_1(\vec{k})\,\langle \chi_{\vec{p}\,'}, e_{\vec{k}\,'}|H_{\rm int}|\chi_{\vec{p}}, e_{\vec{k}}\rangle \tag{3.37}$$

$$= CV\int\int \frac{d^3k'd^3k}{(2\pi)^3}\tilde{\psi}_2^*(\vec{k}\,')\tilde{\psi}_1(\vec{k})\mathcal{M}_{\rm free}(q,v)\delta^3(\vec{k}+\vec{q}-\vec{k}\,') \tag{3.38}$$

$$= CV\mathcal{M}_{\rm free}(q,v)\int \frac{d^3k}{(2\pi)^3}\tilde{\psi}_2^*(\vec{k}+\vec{q})\tilde{\psi}_1(\vec{k}). \tag{3.39}$$

The momentum integral in the above expression contains all the information on the bound electron wave functions, and it is therefore suitable to define it as the *atomic form factor* $f_{1\to2}(\vec{q})$:

$$f_{1\to2}(\vec{q}) = \int \frac{d^3k}{(2\pi)^3}\tilde{\psi}_2^*(\vec{k}+\vec{q})\tilde{\psi}_1(\vec{k}) = \int d^3x\psi_2^*(\vec{x})\psi_1(\vec{x})e^{i\vec{q}\cdot\vec{x}}, \tag{3.40}$$

where the last expression is obtained by Fourier transformation. Comparing the scattering amplitudes for the free electron and the bound electron case, equations (3.35) and (3.39), one sees that the difference is accounted for by making the replacement

$$(2\pi)^3\delta^3(\vec{p}+\vec{k}-\vec{k}\,'-\vec{p}\,') \to V|f_{1\to2}(\vec{q})|^2. \tag{3.41}$$

Through this transformation combined with the fact that only one final electron state is considered, so that $V\int d^3k'/(2\pi)^3 \to 1$, the free cross section in equation (3.34) turns into the cross section to be used in direct detection;

$$\sigma_{1\to2} = \frac{1}{v_{\rm rel}}\int \frac{d^3q}{(2\pi)^3}\frac{1}{16E'_\chi E_\chi E'_e E_e}2\pi\delta(E_i-E_f)\overline{|\mathcal{M}_{\rm free}(q,v)|^2}|f_{1\to2}(\vec{q})|^2. \tag{3.42}$$

This expression can however be simplified by expanding the energy expressions. In the non-relativistic regime,

$$E_i = m_\chi + m_e + \frac{m_\chi v^2}{2} + E_{e,1} \tag{3.43}$$

$$E_f = m_\chi + m_e + \frac{|m_\chi\vec{v}-\vec{q}|^2}{2m_\chi} + E_{e,2} \tag{3.44}$$

$$E_i - E_f = -\frac{q^2}{2m_\chi} + \vec{v}\cdot\vec{q} - E_d, \tag{3.45}$$

where $E_{e,1}$ and $E_{e,2}$ are the electron energies at level 1 and 2, and $E_d \equiv E_{e,2} - E_{e,1}$ is the total energy deposited to the electron. Substituting this into the expression for $\sigma_{1\to2}$, along with the approximation of particle energy $\sim$ particle mass, yields the final cross section

$$\sigma_{1\to 2} = \frac{1}{v_{\text{rel}}} \frac{1}{16 m_\chi^2 m_e^2} \int \frac{d^3q}{4\pi^2} \delta\left(\vec{v}\cdot\vec{q} - \frac{q^2}{2m_\chi} - E_d\right) \overline{|\mathcal{M}_{\text{free}}(q,v)|^2} |f_{1\to 2}(\vec{q})|^2. \tag{3.46}$$

3.2.3 Scattering rate

We can now plug in equation (3.46) in the scattering rate given in equation (3.33):

$$R_{1\to 2} = \frac{\rho_\chi}{16 m_\chi^3 m_e^2} \int d^3v g_\chi(\vec{v}) \int \frac{d^3q}{4\pi^2} \delta\left(\vec{v}\cdot\vec{q} - \frac{q^2}{2m_\chi} - E_d\right) \overline{|\mathcal{M}_{\text{free}}(q,v)|^2} |f_{1\to 2}(\vec{q})|^2. \tag{3.47}$$

The integral over d^3v can be used to eliminate the delta function if the velocity distribution is approximated as spherically symmetric from the lab frame. This is however not the case – the signal rate of a direct detection experiment will depend on the orientation of the target with respect to the galaxy, which changes as the Earth rotates around the sun [2]. Here, this dependence is ignored in order to simplify the calculations.

The delta function in equation (3.47) can be rewritten as

$$\delta\left(\vec{v}\cdot\vec{q} - \frac{q^2}{2m_\chi} - E_d\right) = \delta\left[qv\left(\cos\theta_{qv} - \frac{1}{v}\left(\frac{q}{2m_\chi} + \frac{E_d}{q}\right)\right)\right] = \frac{1}{qv}\delta\left(cos\theta_{qv} - \frac{v_{\min}}{v}\right), \tag{3.48}$$

with θ_{qv} being the angle between $\vec{v}$ and $\vec{q}$, and $v_{\min}$ is the minimum dark matter velocity required to deposit an energy E_d to the electron from equation (3.29). By approximating the velocity integral as spherically symmetric and substituting $g_\chi(\vec{v})$ with the average velocity distribution of all solid angles, $g_\chi(v)$;

$$g_\chi(v) = \frac{1}{4\pi} \int d\Omega g_\chi(\vec{v}), \tag{3.49}$$

the scattering rate now becomes

$$R_{1\to 2} = \frac{\rho_\chi}{64\pi^2 m_\chi^3 m_e^2} \int \frac{d^3q}{q} \int_0^{2\pi} d\phi_v \int v^2 dv \frac{g_\chi(v)}{v} \int_{-1}^{1} d(\cos\theta_{qv}) \delta\left(\cos\theta_{qv} - \frac{v_{\min}}{v}\right) \times \overline{|\mathcal{M}_{\text{free}}(q,v)|^2} |f_{1\to 2}(\vec{q})|^2. \tag{3.50}$$

When simplified this expression can again be written in terms of the vector valued velocity integral:

$$R_{1\to 2} = \frac{\rho_\chi}{128\pi^2 m_\chi^3 m_e^2} \int \frac{d^3q}{q} |f_{1\to 2}(\vec{q})|^2 \int d^3v \frac{g_\chi(\vec{v})}{v} \overline{|\mathcal{M}_{\text{free}}(q,v)|^2} \Theta(v - v_{\min}), \tag{3.51}$$

with $v_{\min}(q, E_d) = E_d/q + q/(2m_\chi)$ and Θ being the Heaviside step function, originating from the delta function constraining $v_{\min}/v < \text{Max}[\cos\theta_{qv}] = 1$.

3.2.4 Ionization form factor

The scattering rate given above depends on the atomic form factor, $f_{1\to 2}$, defined in equation (3.40). This form factor will look different for different detectors, since it depends on the electron wave functions in the target. When the detector target material is a liquid noble gas, like argon or xenon, the form factor can be calculated by treating the electrons as initially bound in spherical atomic potentials and ionized to free particle states at asymptotically large radii. The outgoing electrons have momentum k' and thus recoil energy $E_r = k'^2/2m_e$. Their wave functions are labeled with k', l', m' where l' and m' are angular quantum numbers, and normalized as

$$\langle\tilde{\psi}_2|\tilde{\psi}_1\rangle \equiv \langle\tilde{\psi}_{k'l'm'}|\tilde{\psi}_{klm}\rangle = (2\pi)^3\delta_{l'l}\delta_{m'm}\frac{1}{k^2}\delta(k-k'). \tag{3.52}$$

Ionizing an atom can give rise to a wide range of different ionized electron states, all of which must be taken into account in the scattering rate. Hence, the different angular quantum numbers must be summed over and the final momentum distribution integrated over. At asymptotically large radii the ionized electron phase space takes the free spherical-wave form of

$$\sum_{l'm'}\int\frac{k'^2dk'}{(2\pi)^3} = \frac{1}{2}\sum_{l'm'}\int\frac{k'^3d\ln E_r}{(2\pi)^3}. \tag{3.53}$$

Since the argument of the logarithm must be dimensionless, E_r is now assumed to be divided by some reference value in eV, like αm_e. Besides summing over all final electron states, it is also necessary to sum over all initially occupied states, since it is possible to ionize electrons from different shells. These occupied states are labelled with the quantum numbers n, l, m. Inserting these configurations in equation (3.51), and replacing d^3q with the spherical momentum shell $4\pi q^2dq$, yields

$$\begin{aligned} R_{nlm\to k'l'm'} = \frac{\rho_\chi}{128\pi^2 m_\chi^3 m_e^2}\sum_{nlm}\sum_{k'l'm'}\int d\ln E_r\int 2\pi q dq\frac{k'^3}{(2\pi)^3}|f_{nlm\to k'l'm'}(\vec{q})|^2 \\ \times\int d^3v\frac{g_\chi(\vec{v})}{v}\overline{|\mathcal{M}_{\text{free}}(q,v)|^2}\Theta(v-v_{\min}). \end{aligned} \tag{3.54}$$

It is important to remember that E_d is the total deposited energy, consisting of both the binding energy E_b^{nl} and the electron recoil energy E_r.

We can now redefine the ionization form factor for an electron in the (n,l)-shell, thus generating

the final expression for the ionization scattering rate:

$$\frac{dR_{\text{ion}}}{d\ln E_r} = \frac{\rho_\chi}{128\pi m_\chi^3 m_e^2}\sum_{nl}\int qdq|f_{\text{ion}}^{nl}(k',q)|^2\int d^3v\frac{g_\chi(\vec{v})}{v}\overline{|\mathcal{M}_{\text{free}}(q,v)|^2}\Theta(v-v_{\text{min}}(q,E_b^{nl},E_r)), \quad (3.55)$$

$$|f_{\text{ion}}^{nl}(k',q)|^2 = \frac{4k'^3}{(2\pi)^3}\sum_{l'}\sum_{mm'}\left|\int d^3x\tilde{\psi}^*_{k'l'm'}(\vec{x})\psi_{nlm}(\vec{x})e^{i\vec{q}\cdot\vec{x}}\right|^2. \quad (3.56)$$

In this ionization form factor, an extra factor of 2 has been included to account for the spin degeneracy.

What we need next, is analytic expressions for the wave functions in the above form factor. Following [40], we can express the initial and final electron wave functions as compositions of angular dependant spherical harmonics Y_{lm} and radial wave functions denoted by $\mathcal{R}$:

$$\psi_{nlm} = \mathcal{R}_{nl}(r)Y_{lm}(\theta,\phi), \quad \tilde{\psi}_{k'l'm'} = \tilde{\mathcal{R}}_{k'l'}(r)Y_{l'm'}(\theta,\phi). \quad (3.57)$$

To rewrite the ionization form factor in equation (3.56) in terms of spherical harmonics and radial wave functions we also need to express the exponential in spherical harmonics. These orthogonal harmonic functions then combine in what is called the Wigner 3j-symbol, an alternative to the Clebsch-Gordan coefficients that describes the addition of angular momentum in quantum mechanics (in brackets in the equation below). The final expression for the ionization form factor is

$$|f_{\text{ion}}^{nl}(k',q)|^2 = \frac{4k'^3}{(2\pi)^3}\sum_{l'}\sum_{L=|l-l'|}^{l+l'}(2l+1)(2l'+1)(2L+1)\begin{bmatrix} l & l' & L \\ 0 & 0 & 0\end{bmatrix}^2\left|\int r^2dr\tilde{\mathcal{R}}^*_{k'l'}(r)\mathcal{R}_{nl}(r)j_L(qr)\right|^2, \quad (3.58)$$

where j_L is a spherical Bessel function. The full derivation of this expression is found in Appendix A.

The initial radial wave functions $\mathcal{R}_{nl}$ are given by Roothaan-Hartree-Fock (RHF) wave functions:

$$\mathcal{R}_{nl}(r) = a_0^{-3/2}\sum_j C_{jln}\frac{2Z_{jl}^{n'_{jl}+1/2}}{\sqrt{(2n'_{jl})!}}\left(\frac{r}{a_0}\right)^{n'_{jl}-1}e^{-Z_{jl}r/a_0}. \quad (3.59)$$

Here C_{jln}, Z_{jl} and n'_{jl} are coefficients given by [50] and a_0 is the Bohr radius, ensuring that the ionization form factor is dimensionless. The RHF method is to write the wave functions as finite superpositions of Slater-type orbitals, where C_{jln} are orbital expansion coefficients, Z_{jl} are orbital exponents and n'_{jl} are the principal quantum numbers of the orbitals. These coefficients are tabulated for each element in [50].

The final electron wave functions are continuum-state solutions to the Schrödinger equation with

potential $-Z_{\text{eff}}/r$. $\tilde{\mathcal{R}}_{k'l'}(r)$ is given in [51] as:

$$\tilde{\mathcal{R}}_{k'l'}(r) = 4\pi(2k'r)^{l'} \frac{\left|\Gamma\left(l'+1-\frac{iZ_{\text{eff}}}{k'a_0}\right)\right| e^{\pi Z_{\text{eff}}/(2k'a_0)}}{(2l'+1)!} e^{-ik'r} F_1\left(l'+1+\frac{iZ_{\text{eff}}}{ka_0}, 2l'+2, 2ik'r\right), \quad (3.60)$$

where F_1 is a hypergeometric function of first order. Z_{eff} is determined through treating $\mathcal{R}_{nl}$ as a bound state of a pure Coulomb potential $-Z^{nl}_{\text{eff}}/r$, so that the energy eigenvalue of each nl-shell can be matched to the RHF eigenvalue. For a shell nl with a binding energy of E^{nl}_b eV, Z^{nl}_{eff} is

$$13.6\frac{(Z^{nl}_{\text{eff}})^2}{n^2} = E^{nl}_b \quad \Rightarrow \quad Z^{nl}_{\text{eff}} = n\sqrt{\frac{E^{nl}_b}{13.6}}. \quad (3.61)$$

3.2.5 Crystal form factor

If the detector target is instead a semiconductor crystal, such as germanium or silicon, the electron wave functions and hence the atomic form factor differ quite a lot from the ionization form factor. Instead of electrons being ionized in a liquid noble gas, semiconductor electrons are excited from the valence band to the conduction band. The energy gap separating the occupied valence band from the unoccupied conduction band sets the threshold on the detectable energy range: in order to give rise to a signal, the deposited energy to the electron must be greater than this energy gap.

The band structure in the the periodic lattice of a crystal is complicated, and requires some solid state physics to be accurately described. However, the crystal form factor is derived in a way similar to the ionization form factor; by summing all possible initial and final electron energy states and computing the corresponding electron wave functions. I will give an overview of this derivation, although not as detailed as the one for the ionization form factor. The simple reason for this is that the crystal form factors will not be calculated numerically in this project, but instead looked up in tables. The derivation, as well as the tabulated values, are originally made by [39].

In the periodic potential of a semiconductor crystal, electron wave functions are in Bloch form. This means that all solutions are characterized by the behaviour in the first Brillouin Zone (BZ), the primitive cell in the reciprocal lattice space. The unit normalized wave function of an electron in a given energy state, labelled by band index i and wave vector $\vec{k}$, are

$$\psi_{i\vec{k}}(\vec{x}) = \frac{1}{\sqrt{V}} \sum_{\vec{G}} u_i(\vec{k}+\vec{G}) e^{i(\vec{k}+\vec{G})\cdot\vec{x}}, \quad (3.62)$$

where V is the volume of the crystal, u_i is a periodic function and $\vec{G}$ is the reciprocal lattice vector. These reciprocal lattice vectors correspond to the potential scattering processes in the crystal. Inserting this expression in the general form factor equation (3.40), to get the transition from the initial valence band $\{i\vec{k}\}$ to the final conduction band $\{i'\vec{k}'\}$, yields

$$|f_{i\vec{k}\to i'\vec{k}'}|^2 = \left|\sum_{\vec{G}\vec{G}'} \frac{(2\pi)^3\delta^3(\vec{k}+\vec{q}-\vec{k}'-\vec{G}')}{V} u_i^*(\vec{k}'+\vec{G}+\vec{G}')u_i(\vec{k}+\vec{G})\right|^2. \tag{3.63}$$

The delta function in the above expression puts a constraint on the momentum transfer q: $q = |\vec{k}'+\vec{G}'-\vec{k}|$.

Besides substituting the atomic form factor with $|f_{i\vec{k}\to i'\vec{k}'}|^2$ in the scattering rate in equation (3.51), we need to sum over all possible initial and final states. This is done through integrating over all k:s and k':s in the first Brillouin Zone for given energy bands, and summing over all bands i and i'. The scattering rate of the crystal will then depend on the crystal volume V, which can be written as $V = V_{\text{cell}}N_{\text{cell}}$, where V_{cell} is the volume of the crystal's unit cell and N_{cell} is the number of cells. By expanding the crystal form factor with delta functions over energy as well, the differential scattering rate can be written as

$$\frac{dR_{\text{crystal}}}{d\ln E_d} = \frac{\rho_\chi N_{\text{cell}}\alpha}{16\pi m_\chi^3}\int d\ln q \frac{E_d}{q}|f_{\text{crystal}}(q,E_d)|^2 \int d^3v \frac{g_\chi(\vec{v})}{v}\overline{|\mathcal{M}_{\text{free}}(q,v)|^2}\Theta(v-v_{\text{min}}(q,E_d)), \tag{3.64}$$

with $|f_{\text{crystal}}(q,E_d)|^2$ defined as

$$\begin{aligned}|f_{\text{crystal}}(q,E_d)|^2 =& \frac{2\pi^2}{\alpha m_e^2 V_{\text{cell}}}\sum_{ii'}\int_{BZ}\frac{V_{\text{cell}}d^3k}{(2\pi)^3}\frac{V_{\text{cell}}d^3k'}{(2\pi)^3}\delta(E_d - E_{i'\vec{k}'}+E_{i\vec{k}}) \\ &\times \sum_{\vec{G}'} q\delta(q-|\vec{k}'-\vec{k}+\vec{G}'|)\left|\sum_{\vec{G}} u_{i'}^*(\vec{k}'+\vec{G}+\vec{G}')u_i(\vec{k}+\vec{G})\right|^2.\end{aligned} \tag{3.65}$$

3.2.6 Dark matter velocity distribution

We have now gone through the squared matrix element and the form factors building up the scattering rate. The last piece that needs to be calculated analytically is the dark matter velocity distribution. The velocity dependant part of the rate is

$$\int d^3v \frac{g_\chi(\vec{v})}{v}\overline{|\mathcal{M}_{\text{free}}(q,v)|^2}\Theta(v-v_{\text{min}}), \tag{3.66}$$

where g_χ is the velocity distribution of dark matter particles in the galactic halo surrounding the Milky Way. $\overline{|\mathcal{M}_{\text{free}}(q,v)|^2}$ are defined in equations (3.22) and (3.23) for the Majorana and Dirac case respectively. They consist of a number of terms, either proportional to v^2 or without any velocity dependence. Therefore, two different velocity integrals will appear in the scattering rate:

$$1. \quad \int d^3v \frac{g_\chi(\vec{v})}{v} \Theta(v - v_{\min}); \tag{3.67}$$

$$2. \quad \int v d^3v g_\chi(\vec{v}) \Theta(v - v_{\min}). \tag{3.68}$$

In the galactic rest frame, $g_\chi(\vec{v})$ is approximated by a Maxwell-Boltzmann distribution cut off at the galactic escape velocity, $v_{\text{esc}} = 600$ km/s:

$$g_\chi(\vec{v}) = \frac{1}{K} e^{\frac{|\vec{v}+\vec{v}_E|}{v_0^2}} \Theta(v_{\text{esc}} - |\vec{v} + \vec{v}_E|). \tag{3.69}$$

Here $v_E = 240$ km/s is the average Earth velocity relative to the dark matter halo, $v_0 = 230$ km/s is the typical dark matter velocity and K is a normalization constant determined through the following constraint:

$$\int g_\chi(\vec{v}) d^3v = 1. \tag{3.70}$$

When analytically solving the integrals in equation (3.67) and (3.68) one must consider the different limits arising from the Heaviside functions. Through expanding the exponential in equation (3.69), one can write this as a function of v and $\cos\theta$, where θ is the angle between the dark matter velocity and the velocity of the Earth:

$$g_\chi(v, \cos\theta) = \frac{1}{K} e^{-(v^2 + v_E^2 - 2vv_E \cos\theta / v_0^2)}. \tag{3.71}$$

The Heaviside function $\Theta\left(v_{\text{esc}} - \sqrt{v^2 - 2vv_E + v_E^2}\right)$ then sets the following constraints:

$$\cos\theta < \text{Min}\left[1, \eta(v)\right], \quad \xi(v) \equiv \frac{v_{\text{esc}}^2 - v^2 - v_E^2}{2vv_E}; \tag{3.72}$$

$$v < v_{\text{esc}} + v_E, \tag{3.73}$$

where $\xi(v) < 1$ for $v > v_{\text{esc}} - v_E$. For the first velocity integral (expressed in spherical coordinates), this entails

$$\int_{v > v_{\min}} v dv \int d\Omega g_\chi(v, \cos\theta) = 2\pi \int_{v > v_{\min}} v dv \int d\cos\theta g_\chi(v, \cos\theta) \tag{3.74}$$

$$= 2\pi \left(\int_{v_{\min}}^{v_{\text{esc}} - v_E} v dv \int_{-1}^{1} d\cos\theta g_\chi(v, \cos\theta) + \int_{v_{\text{esc}} - v_E}^{v_{\text{esc}} + v_E} v dv \int_{-1}^{\xi(v)} d\cos\theta g_\chi(v, \cos\theta) \right). \tag{3.75}$$

The analytic solutions for these integrals, divided in the two scenarios

(a) $v_{\min} < v_{\text{esc}} - v_E$

(b) $v_{\text{esc}} - v_E < v_{\min} < v_{\text{esc}} + v_E$,

are

$$\eta_1 = \begin{cases} \frac{v_0^2\pi}{2v_E K}\left(-4e^{v_{\text{esc}}^2/v_0^2}v_E + \sqrt{\pi}v_0\left[\text{Erf}\left(\frac{v_{\min}+v_E}{v_0}\right) - \text{Erf}\left(\frac{v_{\min}-v_E}{v_0}\right)\right]\right) & \text{(a)}; \\ \frac{v_0^2\pi}{2v_E K}\left(-2e^{v_{\text{esc}}^2/v_0^2}(v_{\text{esc}} - v_{\min} + v_E) + \sqrt{\pi}v_0\left[\text{Erf}\left(\frac{v_{\text{esc}}}{v_0}\right) - \text{Erf}\left(\frac{v_{\min}-v_E}{v_0}\right)\right]\right) & \text{(b)}. \end{cases} \tag{3.76}$$

For the second integral in equation (3.68), relating to the terms in $\overline{|\mathcal{M}_{\text{free}}(q,v)|^2} \propto v^2$, the analytic solutions are performed in a similar way. The expressions for these solutions, η_2, are given in Appendix A, equation (A.12) and (A.13).

The scattering rates are now fully understood. The differential rates in equations (3.55) and (3.64) can be integrated over the detectable energy range and multiplied with the exposure to form the number of expected signal events in an experiment, N^{exp}. This number of expected signal events will then differ when calculated in a Majorana theoretical framework, where $\overline{|\mathcal{M}_{\text{free}}^M|^2}$ is used, in comparison to a Dirac theoretical framework, where $\overline{|\mathcal{M}_{\text{free}}^D|^2}$ is used. In order to draw any conclusions about how much these two hypotheses will differ, one however needs a statistical analysis where the probabilities of obtaining a specific number of signals given the two different theories are compared. This will be presented in the next chapter, after an overview of the numerical calculation of N^{exp} for argon, xenon and germanium detectors.

4 Numerics and statistics

Below, the numerical calculation of the scattering rates for ionizing electrons in liquid argon and xenon, and for exciting electrons to the conduction band of germanium crystals, is explained. Thereafter the statistical analysis is presented. This analysis is based on background-free likelihood ratios of experimental data that is Monte Carlo simulated under the Majorana and the Dirac hypotheses, with Majorana as the null hypothesis. The discrimination significance for rejecting the null hypothesis was calculated for Dirac-like mock data sets, covering a wide range of the free parameter space. All calculations were done in Mathematica.

4.1 Numerical calculation of event rates

The number of events in the relevant direct detection experiments were calculated numerically from equation (3.25), $N = \xi \int dE dR/dE$, with the differential rates dR/dE given in equation (3.55) for argon and xenon, and in equation (3.64) for germanium. In these expressions, the dark matter density ρ_χ appears. This is a quantity that can be determined from astrophysical observations, and in this thesis a value of ρ_χ =0.4 GeV/cm^3 is used. This is in agreement with for example [39, 40]. The ionization form factor were calculated for argon, whereas the xenon form factor and the crystal form factor of germanium were retrieved from [39]. The velocity integral and the squared matrix elements were calculated analytically and used as input in the numerical calculations of the scattering rate.

4.1.1 Velocity distribution

As described in section 3.2.6, two distinct dark matter velocity integrals appear in the scattering rates; one for the terms in $\overline{|\mathcal{M}_{\text{free}}|^2}$ that have no velocity dependence, and one for the terms that are proportional to v^2. The solutions to these integrals are η_1 and η_2, given in equation (3.76) and (A.12), (A.13). They depend on the minimal velocity required to deposit an energy E_d to the electron, which is a function of transferred momentum q and E_d. In figure 3, η_1 is plotted as a function of deposited energy for different momentum transfers and different dark matter masses. A similar plot of η_2 is found in Appendix B, figure 15.

It is clear in these figures that it is only the heavier dark matter particles that can transfer enough momentum to deposit an energy above $\sim$ 200 eV. This means that the inner shells of argon and xenon, which have binding energies above 200 eV, will only contribute to the scattering process if the dark matter particle has a mass of order GeV or higher. For this reason, only the three top electron shells for argon and the five top shells for xenon were summed over in the ionization form factors. The shells and the binding energies are given in table 2. The argon 2p level and the xenon 4s level were included to ensure that no scattering contributions were lost; they have binding energies above 200 eV.

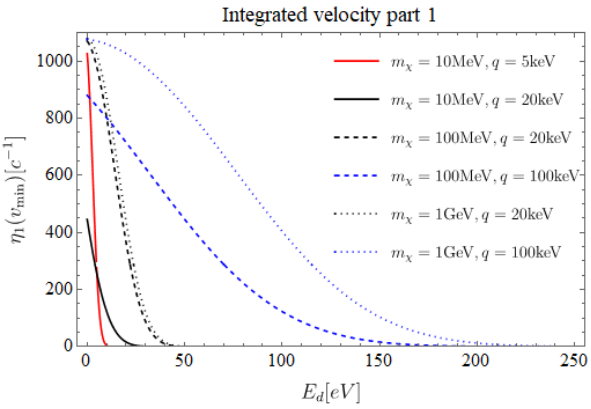

Figure 3: $\eta_1(v_{\min}(q, E_d))$ as a function of deposited energy E_d for different dark matter masses and transferred momenta q. η_1 contains all the dark matter velocity information for the terms in $\overline{|\mathcal{M}_{\text{free}}|^2}$ without velocity dependence. The inner shells of argon and xenon, which have binding energies of $\sim$ 200 eV, only contribute for heavier dark matter particles.

Table 2: Binding energies in eV for the included electron shells of xenon and argon, taken from [40, 52]

Argon	2p	3s	3p		
	248	34.8	16.1		
Xenon	4s	4p	4d	5s	5p
	214	164	75.6	25.7	12.4

4.1.2 Form factors

The form factors for argon were calculated numerically from equation 3.58,

$$|f_{\text{ion}}^{nl}(k', q)|^2 = \frac{4k'^3}{(2\pi)^3} \sum_{l'} \sum_{L=|l-l'|}^{l+l'} (2l+1)(2l'+1)(2L+1) \begin{bmatrix} l & l' & L \\ 0 & 0 & 0 \end{bmatrix}^2 \left| \int r^2 dr \tilde{\mathcal{R}}^*_{k'l'}(r) \mathcal{R}_{nl}(r) j_L(qr) \right|^2,$$

with the radial wave functions given by equations (3.59) and (3.60). Since this form factor was calculated numerically, the integral over r and the sum over final angular quantum number l' had to be cut off at appropriate limits. For large radial distances, the form factor approaches 0 since the initial radial wave function $\mathcal{R}_{nl}(r)$ vanishes. This is shown in figure 4. Therefore, the integral over r was performed from 0 to $7a_0$, where a_0 is the Bohr radius.

To determine the upper limit of the sum over l', the convergence of the ionization form factor was investigated for different cut-offs. This is shown in figure 5, where the ionization form factors for the 3s and 3p level of argon are plotted against the upper limit of l'. The sum was cut off at $l' = 5$.

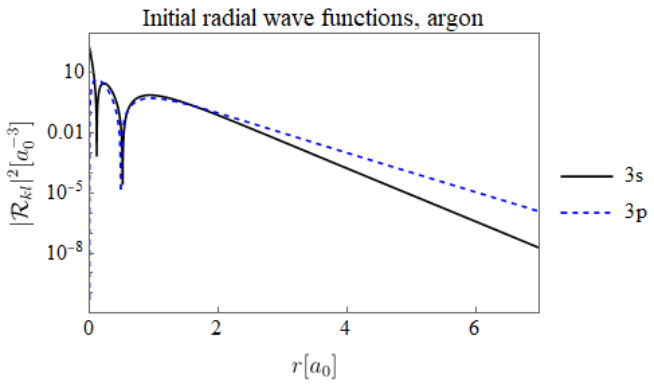

Figure 4: Initial radial wave functions for argon, energy levels 3s and 3p, for different radial distances from the nuclei. The wave functions approaches 0 for a distance of a few a_0:s.

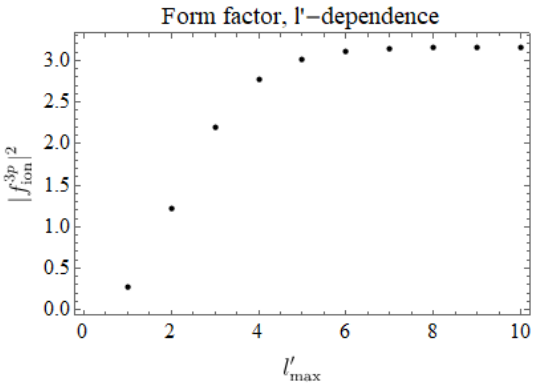

(a) Initial energy level 3p, q =13 keV.

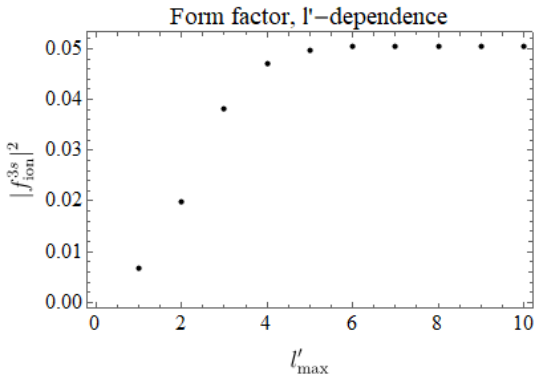

(b) Initial energy level 3s, q = 19keV.

Figure 5: The graphs show how the ionization form factor for argon 3s and 3p depends on the cut-off in the sum over l'. An electron recoil energy of 50 eV was used, and a typical q-value for each energy level, $q = Z_{\text{eff}} \times 4$ keV.

With these cut-offs, the form factors were calculated for the 2p, 3s and 3p level of argon for a range of values of q and k', and then interpolated. 50 values of k' were used, between the corresponding recoil energies $E_r = k'^2/(2m_e)$ of 0.1 eV and 1000 eV. This is in correspondence to the typical size scale explained in section 3.2.1. For q, 50 values in a range between 1 keV and 800 keV were used. This was chosen with equation (3.31) in mind, where it is established that typical transferred momenta are of order keV. In the end, the size of both q and k' depend on the mass of the dark matter particle: heavier particles will induce faster electrons. Thus, the ranges of these variables are set to match the mass scale of light dark matter: from a couple of MeVs to 1 GeV. The form factors for all included electron shells of argon are plotted in figure 6.

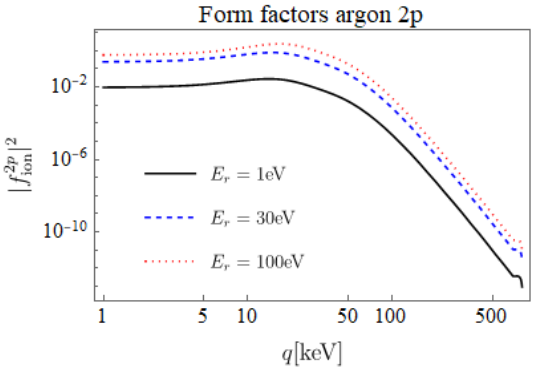

(a) Form factor dependence on q, for given E_r:s.

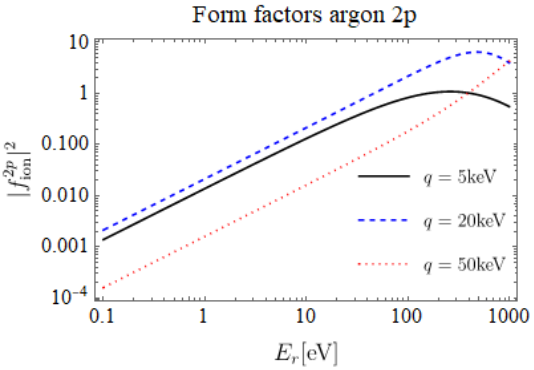

(b) Form factor dependence on E_r, for given q:s.

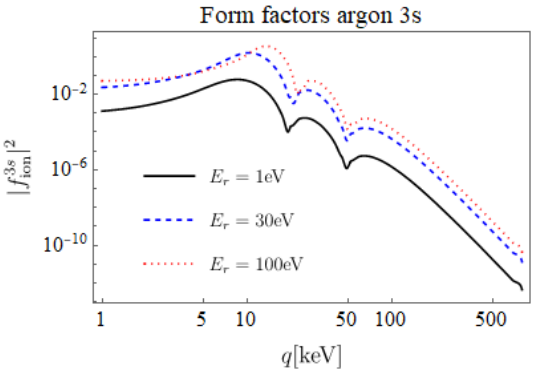

(c) Form factor dependence on q, for given E_r:s.

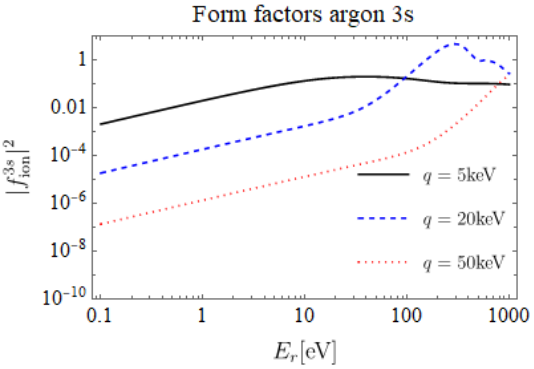

(d) Form factor dependence on E_r, for given q:s.

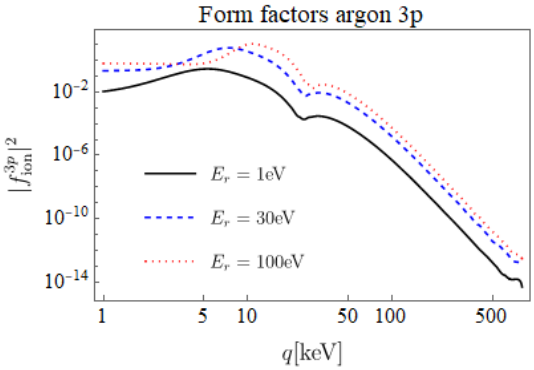

(e) Form factor dependence on E_r, for given q:s.

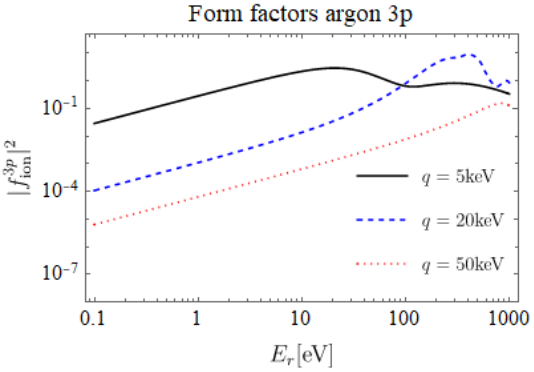

(f) Form factor dependence on E_r, for given q:s.

Figure 6: The graphs show the ionization form factor for argon. (a) and (b) shows the 2p-level, (c) and (d) the 3s-level, (e) and (f) the 3p-level. The graphs to the left are functions of transferred momentum q and the ones to the right are functions of recoil energy E_r.

4.1.3 Matrix elements

The part of the scattering rates that enables discrimination between the Dirac and the Majorana theoretical framework is the modulus square of the matrix elements $\overline{|\mathcal{M}^M_{\text{free}}|^2}$ and $\overline{|\mathcal{M}^D_{\text{free}}|^2}$, given in equations (3.22) and (3.23). They are functions of q and dark matter velocity v. $\overline{|\mathcal{M}^M_{\text{free}}|^2}$ has one term, with the coupling coefficient C_1^2 as free parameter (besides the dark matter mass), and $\overline{|\mathcal{M}^D_{\text{free}}|^2}$ has three terms, with $\{C_1^2, C_2^2, C_3^2\}$ as free parameters. These three parameters have different dimensions: C_1^2 is in $[\text{eV}^{-4}]$ and C_2^2, C_3^2 are in $[\text{eV}^{-2}]$.

When multiplying the terms of $\overline{|\mathcal{M}_{\text{free}}(q,v)|^2}$ with the appropriate velocity integrals, described by $\eta(q, E_d) = \{\eta_1, \eta_2\}$, the result is a function of q only, for a given E_d and m_χ. Thus the potential of distinguishing between Dirac and Majorana dark matter resides in the distinct q-dependence of the terms corresponding to the three coefficients C_1^2, C_2^2 and C_3^2. This q-dependence is shown in figure 7 for different masses and energies. In these graphs, the three curves were obtained through keeping only one non-zero coefficient $C_{i=1,2,3}$ each time.

The expressions for $\overline{|\mathcal{M}_{\text{free}}|^2}$ are quite complicated, with intricate dependence on the dark matter mass, and this gives rise to the large difference between the behaviour of the curves in the separate graphs of figure 7.

4.1.4 Scattering rates and expected events

The last step in the numerical calculation of the differential scattering rates is the integral over transferred momentum q, that appear both in the case of ionization and in the case of excitation of an electron. These integrals were performed over the entire momentum region where the form factors were defined, that is

- 1–800 keV for argon,
- 1.3–200 keV for xenon,
- 0.01–67 keV for germanium.

The band structure of germanium explains the difference in q-intervals in the above list: the possible momentum transfer is of course bigger when ionizing a bound electron than when exciting it to the valence band of a crystal. The differential scattering rates for argon, xenon and germanium are shown in figure 8 as functions of energy.

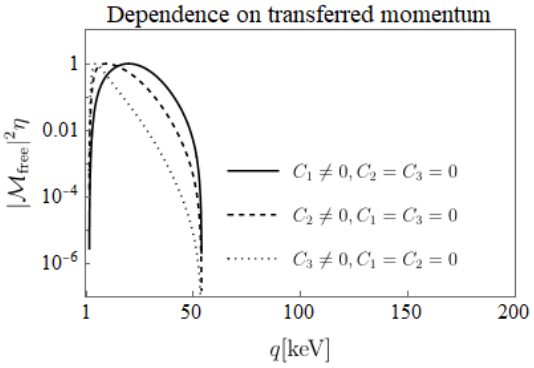

(a) m_χ =10 Mev, E_d =5 eV.

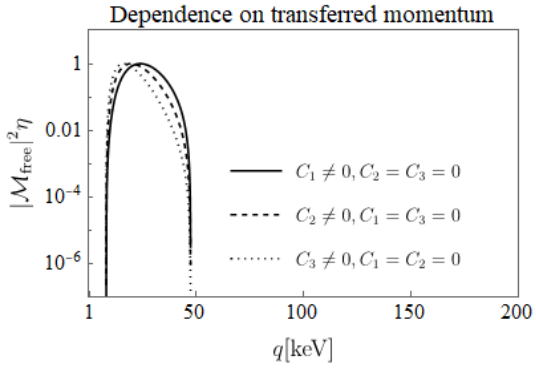

(b) m_χ =10 Mev, E_d =20 eV.

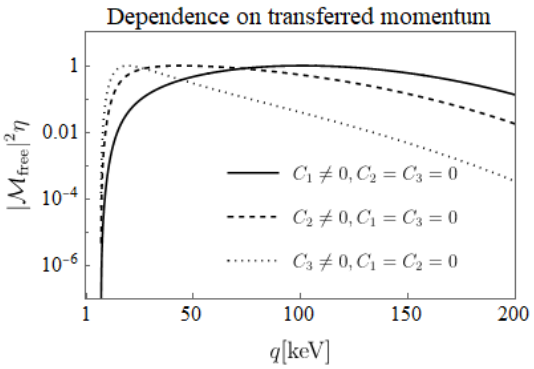

(c) m_χ =50 Mev, E_d =20 eV.

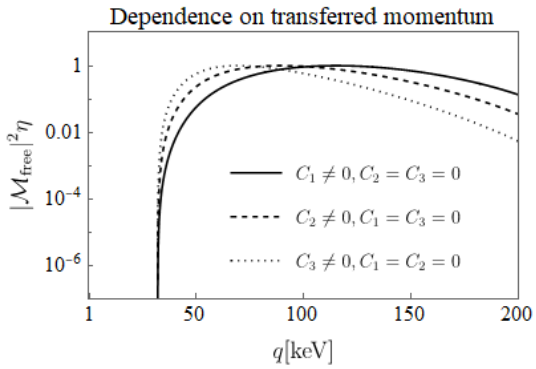

(d) m_χ =50 Mev, E_d =80 eV.

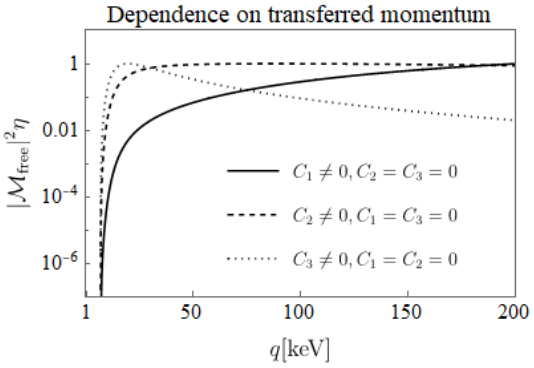

(e) m_χ =200 Mev, E_d =20 eV.

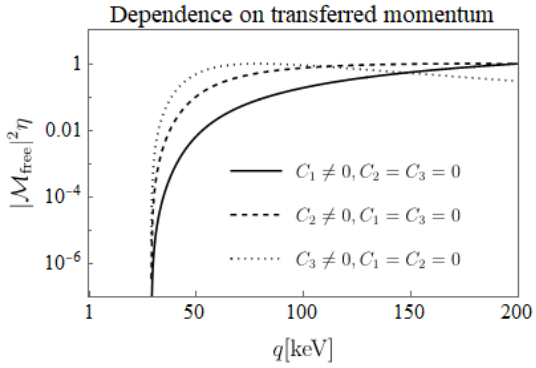

(f) m_χ =200 Mev, E_d =80 eV.

Figure 7: The graphs show the squared matrix elements $\overline{|\mathcal{M}_{\text{free}}|^2}$ multiplied with the integrated dark matter velocity contributions η, as functions of transferred momentum q. The three terms of $\overline{|\mathcal{M}_{\text{free}}|^2}$ are plotted separately and normalized. $C_2 = C_3 = 0$ corresponds to the Majorana amplitude, whereas the Dirac amplitude is a linear combination of all three terms. The four graphs are calculated for different masses and deposited energies. The separation of the curves in each graph determines the chances of discriminating between the Dirac and Majorana hypotheses.

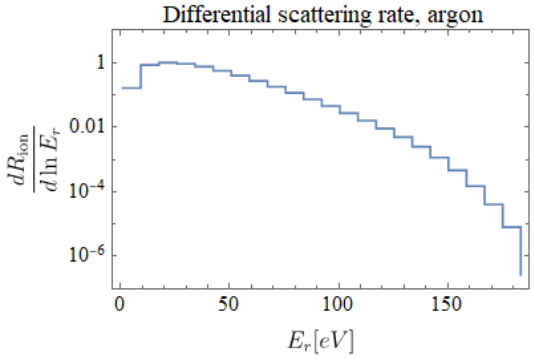

(a) Argon differential rate as function of recoil energy.

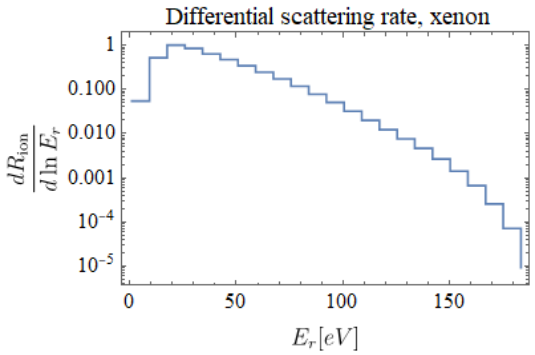

(b) Xenon differential rate as function of recoil energy.

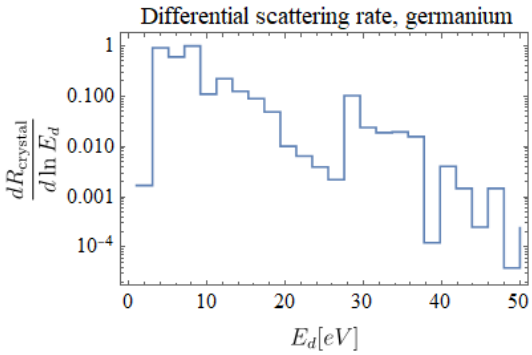

(c) Germanium differential rate as function of deposited energy.

Figure 8: Differential scattering rates for the three different detector targets, plotted as functions of recoil energy E_r for the liquid noble gases, and deposited energy E_d for the semiconductor. In the differential rate, the energy is divided by the reference value αm_e, yielding $\ln E$ dimensionless. All rates are calculated for m_χ =50 MeV and normalized.

These differential rates were then integrated over the kinematically accessible energy region for a given dark matter mass, in energy bins labelled by i. This was done in Mathematica with the trapezoidal method. The number of expected events in each energy bin, N_i^{exp}, was retrieved through multiplying with the exposure ξ;

$$N_i^{\text{exp}} = \xi R_i = \int_{\Delta E_i} d\ln E \frac{dR}{d\ln E}. \tag{4.1}$$

This number of expected events in each energy bin was then used to simulate experimental data, that is, the number of observed events in each energy bin, N_i^{obs}. The total number of signal events, expected or observed, is the sum of all bins: $N = \sum_i N_i$. Together, N_i^{obs} and N_i^{exp} form the basis of the statistical analysis, which will be presented below.

4.2 Statistical analysis

The goal of the statistical analysis is to discriminate between the Dirac and the Majorana theoretical framework. The measure used is the discrimination significance: the certainty with which one can reject the Majorana hypothesis for a Dirac-like data set. The data was Monte Carlo simulated, and the discrimination significance was determined through maximisation of likelihood functions. The statistical procedure, from likelihood to significance, is described below.

4.2.1 The likelihood method

This analysis is founded on background-free likelihood calculations. The maximum likelihood of obtaining a set of data, i.e a number of signal events N^{obs}, can be calculated for the two hypotheses

$$\begin{aligned} H_M: &\text{ Majorana-like dark matter, with free parameters } \Theta_M = (m_\chi, C_1); \\ H_D: &\text{ Dirac-like dark matter, with free parameters } \Theta_D = (m_\chi, C_1, C_2, C_3). \end{aligned}$$

The likelihood is defined as the product of the probabilities of observing a number of signal events N_i^{obs} in an energy interval i, given the theoretically expected number of events N_i^{exp}:

$$\mathcal{L}(d|\Theta) = \prod_i P(N_i^{\text{exp}}(\Theta)|N_i^{\text{obs}}) = \prod_i \frac{N_i^{\text{exp}}(\Theta)^{N_i^{\text{obs}}} e^{-N_i^{\text{exp}}(\Theta)}}{N_i^{\text{obs}}!} \tag{4.2}$$

Here Θ are the free parameters, corresponding either to the Majorana or to the Dirac hypothesis, and d stands for the set of experimental data, that is, $d = \{N_i^{\text{obs}}\}$. If n experiments are combined, then the total likelihood is the product of the likelihoods for each of the experiments:

$$\mathcal{L}(d|\Theta) = \prod_k^n \mathcal{L}_k(d|\Theta). \tag{4.3}$$

A test statistic q can be formed through maximising the likelihood functions with respect to the free parameters for the Majorana and Dirac hypotheses, Θ_M and Θ_D, respectively.

$$q(d) = -2\ln\frac{\mathcal{L}(d|\hat{\Theta}_M)}{\mathcal{L}(d|\hat{\Theta}_D)}, \tag{4.4}$$

where $\hat{\Theta}$ are the optimal parameters. Repeating this for a sample of data sets d will yield a distribution of q-values. Data originating from a Majorana-like dark matter particle will result in one distribution, $f_M(q)$, and data originating from a Dirac-like dark matter particle will result in another distribution $f_D(q)$. The separation of these two distributions determines the discrimination significance.

Thus, both Dirac-like and Majorana-like data sets would need to be created. However, due to the

fact that the Majorana hypothesis is a special case of the Dirac hypothesis (where $C_2 = C_3 = 0$), the Majorana distribution of the test statistic can actually be derived analytically. It is a so called half chi-square-distribution, with two degrees of freedom, one for each parameter constraint.

$$f_D(q) = P(q|d_{\text{Dirac}}) \tag{4.5}$$

$$f_M(q) = \frac{1}{2}\chi^2_2 \tag{4.6}$$

This reduced the number of calculations substantially, since the only data sets actually used were Dirac-like. In lack of any experimental evidence for dark matter, these data sets were Monte Carlo simulated.

4.2.2 Data simulation

The mock data sets in each energy region were obtained through random sampling from a Poisson distribution with mean N_i^{exp}. This number of expected events was calculated for a set of benchmark parameters $\Theta_b = \{m_{\chi,b}, C_{1,b}, C_{2,b}, C_{3,b}\}$. The Poisson distribution is given by

$$P(N_i^{\text{exp}}(\Theta_b)|N_i^{\text{obs}}) = \frac{N_i^{\text{exp}}(\Theta_b)^{N_i^{\text{obs}}} e^{-N_i^{\text{exp}}(\Theta_b)}}{N_i^{\text{obs}}!}. \tag{4.7}$$

These benchmark parameters have to be chosen with care, since they are representing the properties of the dark matter particle captured in the mock experiment. It is important that the total number of expected events does not exceed the current experimental exclusion limits; if the prediction is much higher than what is seen in the measurements, then there is likely something wrong with the prediction.

In statistical language, the number of expected signal events must be inside the 90%-confidence level. This means that 90% of the probability distribution for observing different number of events given the underlying theory, must be in the unexplored area above the experimentally established signal. The upper limit $N_{90\%}^{\text{exp}}$ corresponding to this demand is obtained through solving the equation

$$\sum_{k=(N^{\text{obs}}+1)}^{+\infty} P(N^{\text{exp}} + N^{\text{bg}}|k) = 0.9 \tag{4.8}$$

for N^{exp}. Here N^{bg} is the number of background events in the experiment where N^{obs} is retrieved from.

This $N_{90\%}^{\text{exp}}$ was calculated for the three scattering rates, using the following values from the XENON100 2016 results [52]: an exposure $\xi = 48\text{kg}\times477\text{days}$; number of background events N^{bg} =6.6 events; number of observed events N^{obs} =11 events. This resulted in $N_{90\%}^{\text{exp}}$ =10.0 events. It is possible

to predict a number of signal events that exceeds this limit, if the exposure is raised accordingly. To predict 100 signal events, the exposure would have to be scaled up with a factor of ~ 10.

The total contribution of the benchmark coupling constants for the mock data sets are constrained by demanding a 90%-confidence level of N^{exp} for a given exposure. However, the relative contributions of each coefficient can still vary. The differential scattering rate can be expressed as

$$\frac{dR}{d\ln E} = C_1^2 \left(\Gamma_1 + \frac{C_2^2}{C_1^2}\Gamma_2 + \frac{C_3^2}{C_1^2}\Gamma_3 \right), \tag{4.9}$$

where $\Gamma_{i=1,2,3}$ contains everything but the coupling constants $C^2_{i=1,2,3}$. C_1 can then be set to generate a certain number of expected events for the entire energy region, given an exposure. The ratios C_2/C_1 and C_3/C_1 can vary infinitely, but since C_2 and C_3 are of lower energy dimension than C_1, the ratios should be bigger than 1. Once these ratios are chosen, a mock data set can be randomly sampled from the Poisson distribution. A mock data set for an argon target, with unit coupling ratios and an exposure corresponding to 100 events fulfilling the current 90%-confidence level, is shown in figure 9. In the graph, 100 random samples were used.

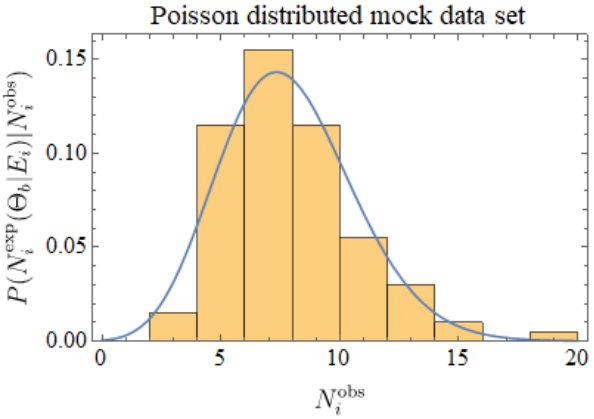

Figure 9: Mock data set for a direct detection experiment with argon target. The data is obtained through random variation of a Poisson distribution of mean $N_i^{\text{exp}}(\Theta_b|E_i) = 7.8$. The energy interval E_i is 3.1–4.7 eV and the benchmark parameters Θ_b are $m_{\chi,b}$ =50 MeV, $C_{2,b}/C_{1,b} = C_{3,b}/C_{1,b} = 1$ and $C^2_{1,b} = 0.007$ (set to generate 100 events in total energy region). The histogram shows the probability distribution of 100 random samples of observed events N^{obs}, and the curve is the analytic Poisson probability distribution.

4.2.3 Discrimination significance

Once the mock data sets are generated, the distributions of q-values for the Dirac and the Majorana hypothesis can be computed through maximising the likelihood functions. This maximisation was done with respect to the coupling constants, for fixed dark matter masses. The calculation was performed

with the NMaximize-function in Mathematica. A global optimisation method based on differential evolution was chosen, and the optimisation performance was tested for different settings, to ensure that the global maximum was found.

In this way, the Dirac-like distribution $f_D(q)$ was generated. Combined with the analytic distribution $f_M(q)$ representing the Majorana-like dark matter data sets, this leads to a so called p-value. p is the probability of observing a q-value from a set of Majorana data, that is greater than $q_{\text{med},D}$, the median of $f_D(q)$:

$$p = \int_{q_{\text{med},D}} f_M(q)dq. \tag{4.10}$$

Hence the p-value is a measure on how separated the two distributions f_M and f_D are. This is shown graphically in figure 10, where graph (a) is the probability distribution of q generated from a Dirac-like mock data set, and graph (b) is the half chi-square distribution of q representing the Majorana hypothesis.

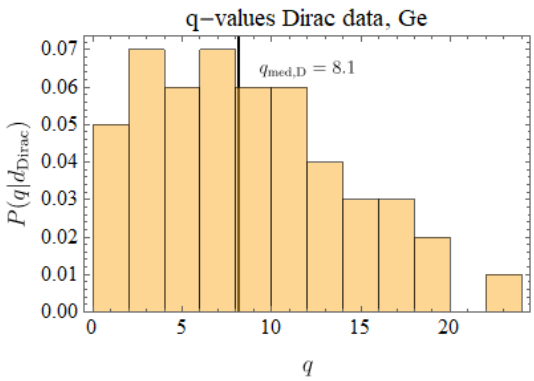

(a) Probability distribution of 100 randomly generated q-values from Dirac-like mock germanium data set.

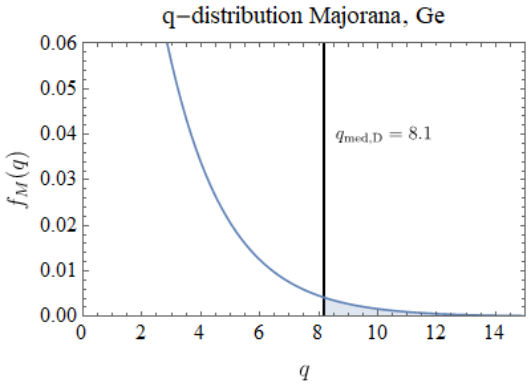

(b) Analytic probability distribution f_M corresponding to Majorana-like mock data sets. The p-value is the blue shaded area to the right of $q_{\text{med,D}}$

Figure 10: Calculation of p-value. p is the probability of observing a q-value from a set of Majorana data, that is greater than the median of $f_D(q)$, which is marked in both graphs. Graph (a) shows the random variation of $f_D(q)$ made from Dirac-like mock data sets, and graph (b) shows the analytic probability distribution $f_M(q)$ that substitutes the Majorana-like mock data sets. The p-value is the filled area in graph (b).

When translating the probability p to a Gaussian distribution $G(x)$ of mean 0 and standard deviation 1, a discrimination significance z can be obtained. The discrimination significance is the distance from the peak of the normal distribution to the vertical line that separates the probability p from $1 - p$. It is the quantile corresponding to the probability $1 - p$, calculated through the inverse of the cumulative distribution function Φ that sums up all the probabilities in a given distribution:

$$\Phi(z) = \int_{-\infty}^{z} dx G(x) = (1-p) \quad \Rightarrow \quad z = \Phi^{-1}(1-p). \tag{4.11}$$

Figure 11 shows the z-value graphically.

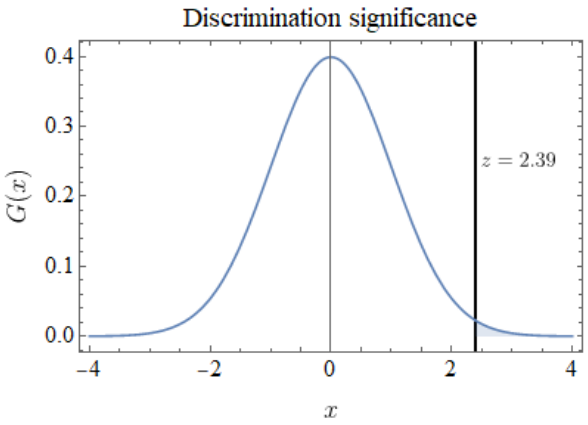

Figure 11: The discrimination significance z is the distance from the mean of the normal distribution to the contour of the probability p. The blue shaded area to the right of z is the p-value from figure 10.

If the Gaussian distribution has standard deviation 1, the discrimination significance z can be interpreted in terms of standard deviations. It is a measure of how unlikely it is to find a Dirac-like dark matter signal, if the Majorana hypothesis is true. A high discrimination significance corresponds to a rejection of the Majorana hypothesis: if a potential experimental data set of the future is alike to the Dirac-simulated data, then the Majorana nature can be discarded based on this test. If the experimental data is instead alike to Majorana-simulated data, it will be impossible to draw any conclusions about the particle/antiparticle nature. All this is of course provided that the rest of the theoretical framework resembles reality – for instance, that dark matter interacts with photons according to this particle model.

The discrimination significance was calculated for a range of different Dirac benchmark parameters for each of the three mock experimental targets, to cover as many as possible of the dark matter particle alternatives, within the given theoretical framework. The results of this are shown in the following chapter.

5 Results

One major result of this study is a purely theoretical one: the fact that dark matter-electron scattering processes ruled by the general, spin independent Lagrangian of equation (3.13),

$$\mathcal{L}_{SI} = C_e \bar{\psi}_\chi \psi_\chi \bar{\psi}_e \psi_e + C_o \bar{\psi}_\chi \gamma_\mu \psi_\chi \bar{\psi}_e \gamma^\mu \psi_e,$$

entail no possibility to distinguish between Dirac and Majorana dark matter in a direct detection experiment. This was shown in section 3.1.2, by a comparison of the Dirac and Majorana cross sections derived from the above Lagrangian. It turned out that the Dirac cross section can always be mapped to the Majorana cross section, making it impossible to separate the two for a given set of experimental data. Discrimination between Dirac and Majorana dark matter is however possible for photon mediated interactions.

5.1 Coupling parameter grid

In the dark matter-photon framework, the discrimination significance was calculated for argon, xenon and germanium targets. A large part of the parameter space for each experimental setup was explored. The benchmark masses used were 10 MeV, 50 MeV and 200 MeV, and the benchmark coupling constant ratios C_3/C_1 and C_2/C_1 were varied for each mass. C_1 was set to generate 100 expected events in total, for an exposure about ten times as high as the current 48kg×477 days exposure of XENON100. This exposure was fixed to fulfil the 90%-confidence level of the number of signal events. The variation of the coupling constant ratios was made with a parameter grid covering six orders of magnitude for each ratio, starting from 1 and rising.

The result of this is shown in figure 12 for m_χ =10 MeV, figure 13 for m_χ =50 MeV, and figure 14 for m_χ =200 MeV. In these graphs, a common colour scheme is used. The white parts of the graphs correspond to infinite discrimination significances. Since all calculations were done numerically in Mathematica, these values are simply higher than the available computational precision. The points on the grid where this occurs correspond to very high C_3^2/C_1^2-ratios.

For a dark matter mass of 10 MeV, shown in figure 12, the argon target does not yield any significance above four standard deviations, and the germanium and xenon targets have quite broad regions with high significance. For the benchmark mass 50 MeV, figure 13 shows that the discrimination prospects for argon and xenon targets are quite similar, whereas the prospects for germanium targets differ. For the liquid noble gases, a large part of the parameter space yields a significance < 2, but the significance reaches arbitrary high values in the corners of the parameter grid. On the contrary, a large part of the parameter space accessible for germanium targets yields a significance of a couple of standard deviations, but the maximum significance is lower than for argon and xenon. Finally, for

m_χ =200 MeV, in figure 14, germanium still has a broad region of medium high significance and argon a narrow region of high significance, but xenon only has a narrow region of medium significance.

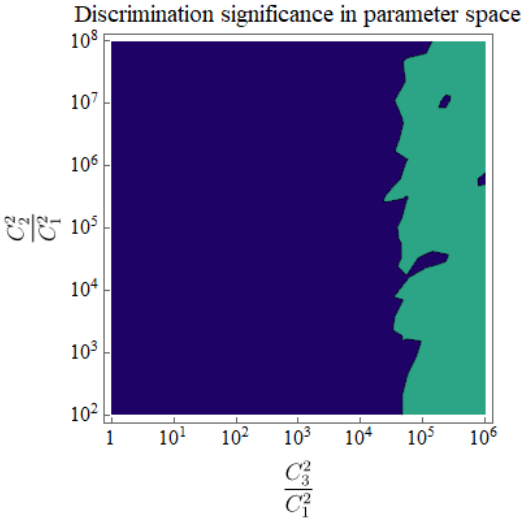

(a) Argon target, m_χ =10 MeV.

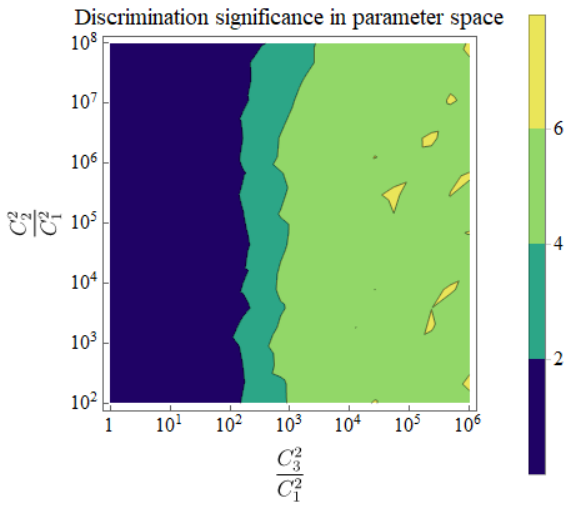

(b) Germanium target, m_χ =10 MeV.

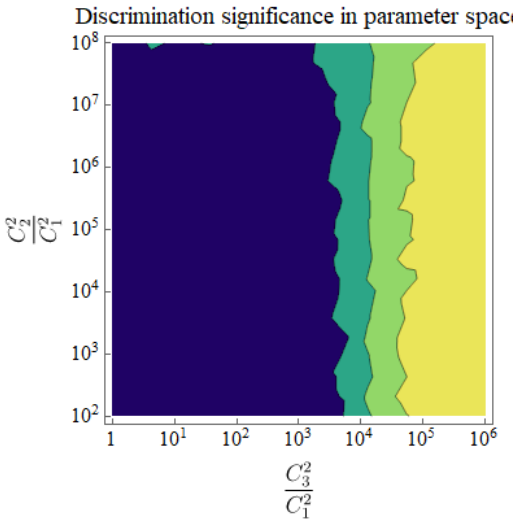

(c) Xenon target, m_χ =10 MeV.

Figure 12: The graphs show the discrimination significance for rejection of the Majorana hypothesis given Dirac-like mock data sets, with dark matter mass m_χ =10 MeV and different parameter ratios C_3^2/C_1^2 and C_2^2/C_1^2. C_1 is set to generate in total 100 events in each experiment, which corresponds to the 90%-confidence level signal for an exposure ten times as much as the current XENON100 value. The four graphs differ in experimental setups. The colour scheme for all graphs is shown in the up right corner.

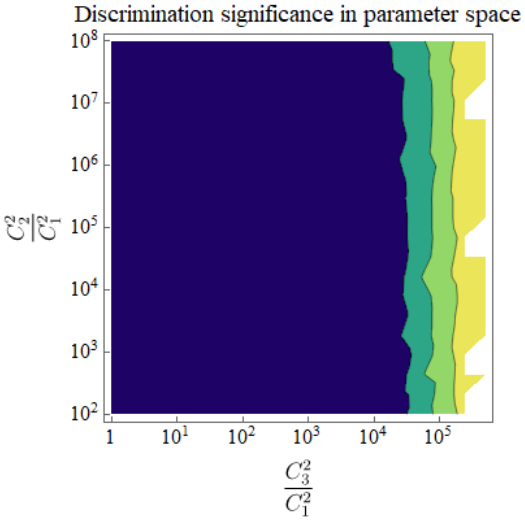

(a) Argon target, m_χ =50 MeV.

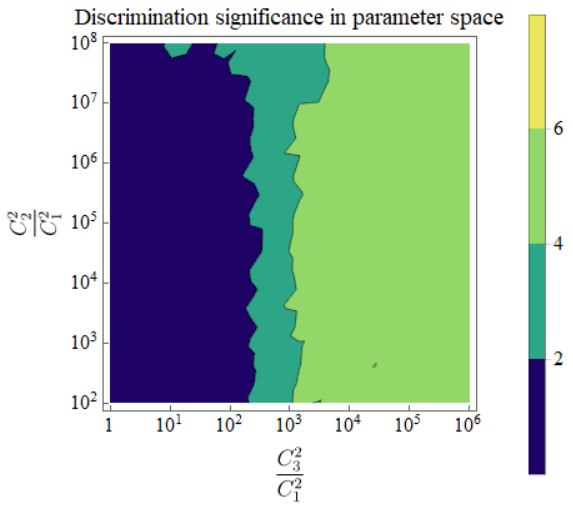

(b) Germanium target, m_χ =50 MeV.

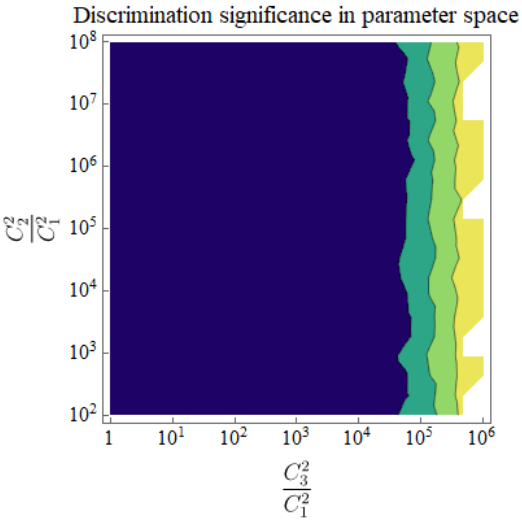

(c) Xenon target, m_χ =50 MeV.

Figure 13: The graphs show the discrimination significance for rejection of the Majorana hypothesis given Dirac-like mock data sets, with dark matter mass m_χ =50 MeV and different parameter ratios C_3^2/C_1^2 and C_2^2/C_1^2. C_1 is set to generate in total 100 events in each experiment, which corresponds to the 90%-confidence level signal for an exposure ten times as much as the current XENON100 value. The four graphs differ in experimental setups. The colour scheme for all graphs is shown in the up right corner. The white parts of the graphs represent an infinite discrimination significance.

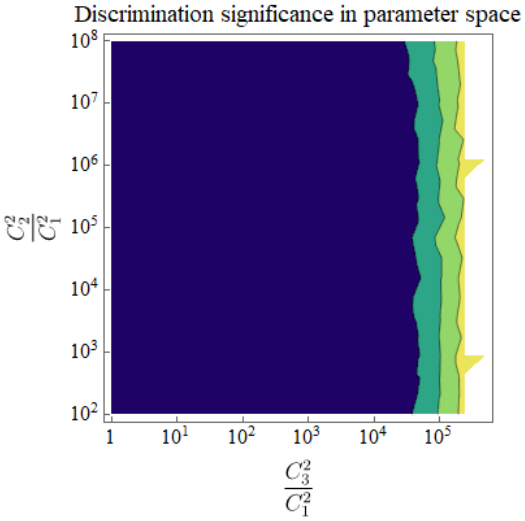

(a) Argon target, m_χ =200 MeV.

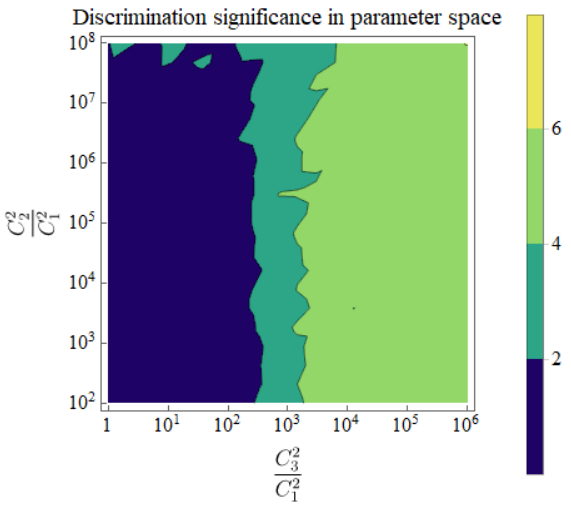

(b) Germanium target, m_χ =200 MeV.

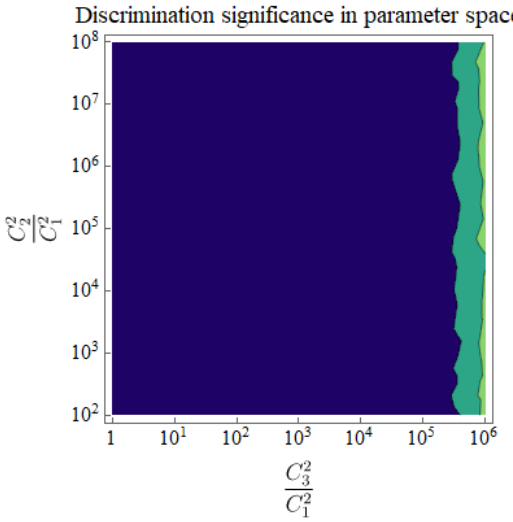

(c) Xenon target, m_χ =200 MeV.

Figure 14: The graphs show the discrimination significance for rejection of the Majorana hypothesis given Dirac-like mock data sets, with dark matter mass m_χ =200 MeV and different parameter ratios C_3^2/C_1^2 and C_2^2/C_1^2. C_1 is set to generate in total 100 events in each experiment, which corresponds to the 90%-confidence level signal for an exposure ten times as much as the current XENON100 value. The four graphs differ in experimental setups. The colour scheme for all graphs is shown in the up right corner. The white parts of the graphs represent an infinite discrimination significance.

5.2 Number of random samples

In the parameter grid calculations, the mock data sets, from which f_D was created, consisted of 20 random samples. The number of samples was chosen mainly to save computing time. For a fixed set of benchmark parameters, the discrimination significance was calculated 20 times to check the variation between the randomly sampled data sets. The result of this is shown in table 3. The standard deviation of the significance diminishes with larger data sets, but this statistical uncertainty was traded off against computing time.

Sample size	Mean(z)	Std(z)
20	5.00	0.23
50	4.95	0.13
100	4.98	0.06

Table 3: Mean value and standard deviation (Std) of the discrimination significance z calculated 20 times with the same benchmark parameters. The number of random samples used in each calculation were varied, to investigate the statistical uncertainty in small data sets.

6 Discussion

The discrimination significance of rejecting the Majorana hypothesis differs between the three types of detector targets, as well as between the benchmark dark matter masses. The reason for these differences is to be found in the kinematically available energy and momentum ranges for the different targets. Since the discrimination procedure relies on the distinct q-dependence of the Dirac and Majorana scattering amplitudes, the discrimination significance will depend on the region of transferred momentum where scattering events can be detected. This is tightly bound to the observable electron energy region.

Germanium detectors have a lower detectable energy region than argon and xenon detectors do, due to the low band gap of semiconductor materials. This means that germanium detectors are more sensitive to lighter dark matter masses, as explained in section 3.2.1. The germanium form factors also fall off fast with deposited energies, making the high-momentum part of the spectrum unavailable [39]. Looking at figure 7, where the q-dependence of the separate scattering amplitude terms are shown, this means that only the separation between the curves for lower q-values (below $\sim$70 keV) contributes to the germanium discrimination significance. For argon and xenon, the entire q-range contributes.

For m_χ =10 MeV, the entire scattering amplitude is below the germanium threshold, and it is also for this benchmark mass that the germanium significance reaches its maximum value (see figure 12 (b)). Argon, on the contrary, has very low significances for this mass. With a top shell binding energy of 16 eV, this mass is close to the low-energy detection threshold for argon. It is also clear from figure 7 (b) that the separation of the Dirac and Majorana squared matrix elements is quite small for $E_d = 20$, which would be accessible to argon detectors. Xenon, which has a top shell binding energy of 12 eV, performs better with this light mass.

For the higher masses, the q-regions that are kinematically unavailable for germanium suppresses its maximum significance, since the largest separation between the scattering amplitude terms appear in the high q-end of the spectrum. Thus the highest significance values are found with argon (and for m_χ =50 MeV also xenon) targets. These high values are though restricted to narrow coupling parameter regions (See figure 13 (a), (c) and 14 (a)). This might be explained by the crossing of the curves in figure 7 – including the entire q-region at first leads to cancellation of the Dirac and Majorana differences, although the best discrimination outlooks await in the end of the spectrum. The cut-off in q for germanium targets results in broader regions with medium high significance: the cancellation does not occur, but the highest significances are out of reach.

The discrimination significance for all three targets are highly dependent on the ratio C_3/C_1, but not on C_2/C_1. This might be explained partly by figure 7, which show larger separation between the C_3- and C_1-curves than between the C_2- and C_1-curve, and partly on the numerical suppression of C_2 due to the dependence on v^2 (see equation (3.23)).

To sum up, the results are highly dependent on the kinematically available energy region of the target material, but rejection of the Majorana hypothesis in favour of the Dirac hypothesis is possible in some parts of the coupling constant parameter space. These favourable regions are however hard to determine generally, since the scattering amplitudes have intricate dependencies on both the dark matter mass and the transferred momentum. The original discrimination procedure, which was created in a WIMP dark matter-nuclei scattering context [4], resulted in a significance only slightly dependent on the dark matter mass and restricted to a certain parameter region; one where there is partial cancellation between neutron and proton contributions to the total cross section. In the theoretical framework used here it is rather "the more, the merrier" – the larger the ratio of Dirac coupling parameters and Majorana coupling parameters, the higher discrimination significance can be obtained. It can, as we have seen, reach infinity.

There are of course many uncertainties in this investigation. The most major ones are the following:

- *The astrophysical input:* The velocity distribution and the local dark matter density are astrophysical inputs in this thesis, and as such they contribute to the overall uncertainty. The density value ρ_χ =0.4 GeV/cm^3 is the current standard in dark matter research; it has theoretical endorsement (see for example [53]), with estimated deviations of only a few percents. The Maxwell-Boltzmann velocity distribution has received some critique [54], but is nonetheless also the standard approach. However, in this thesis, both the time and the directional dependence of the velocity distribution are neglected. This could alter the scattering rates significantly, see [55] for a quantitative estimation.

- *The atomic form factors:* For argon and xenon, the form factors were calculated from continuum-state solutions to the Schrödinger equation, which according to [40] has better agreement for outer shell electrons than the alternative plane-wave approximation. Still, this is an approximation of the actual bound wave functions. The germanium form factors were taken from [39], who conclude their results to be accurate at the few percents level.

- *The transverse velocity approximation:* The squared matrix elements used in this thesis were derived by neglecting the dark matter-electron transverse velocity dependence on electron momentum. This approximation is not really motivated by anything else than the mathematical simplicity it entails – moreover, the implications for the scattering rates are unknown. It was however not feasible to do otherwise, within the scope of this project.

- *The statistical analysis:* The statistical analysis is based on a median discrimination significance, obtained through maximisation of background-free likelihoods. Since the likelihood is multimodal, a Bayesian analysis, focusing not on the maximum but on the overall distribution of the likelihood, could have rendered a more productive result. Furthermore, the influence of background signals on the observed events could have been taken into account. This approximation is

however not crucial, since the total number of events considered here are well above the current experimental signals. But the statistical analysis could be improved by increasing the number of random samples, which, according to table 3, diminishes the statistical uncertainty. This uncertainty, originating from the low number of samples used in the parameter grid calculations, could for example be the reason for the seemingly random yellow fields in figure 12 (b).

In a more general perspective, this entire discrimination procedure is based on the three following assumptions: 1. That a dark matter signal is found in direct detection experiments; 2. That this signal origins from Dirac-like dark matter, otherwise discrimination is impossible; 3. That the theoretical framework used in this work actually models reality – that is, that dark matter is in the sub-GeV mass region, that it interacts with electrons through the dark matter-photon Lagrangian given in equation (3.19), and that particles and antiparticles contribute equally to the Dirac scattering amplitude. If any of these three conditions are unfulfilled, the prospects of determining the particle/antiparticle nature of dark matter presented here are no longer relevant.

7 Conclusions

In this thesis, the prospects for discrimination between Dirac and Majorana dark matter, interacting with electrons in direct detection experiments with argon, xenon and germanium targets, has been studied. It was shown that scattering processes ruled by the most general Lagrangian, the electron analogy of the dark matter-nuclei Lagrangian used in the original discrimination test made by [4], yields Dirac and Majorana cross sections that are indistinguishable. Therefore, no discrimination based on direct detection is possible in that theoretical framework.

If dark matter instead scatters off detector target electrons through loop level photon interactions, rejection of a Majorana hypothesis given Dirac-like dark matter signals is possible. A large part of the coupling constant parameter space was explored in this framework, for a couple of sub-GeV dark matter masses. It was found that germanium detectors yield discrimination significances above four standard deviations in a broad parameter region, whereas argon and xenon detectors yield corresponding values in a narrow region of very high Dirac to Majorana coupling constant ratios. The discrimination significance is highly dependent on the kinematically available energy region of the detector target.

It is concluded that discrimination between Dirac and Majorana dark matter is theoretically possible in the foreseeable future, given that direct detection signals of Dirac-like dark matter are found, and that the theoretical framework used here is a viable model of reality. This study could be continued by analysing the combination of several experiments, and by extending the analysis to other dark matter masses and other experimental setups, both other direct detection targets and other detection techniques. In a broader perspective, this could help guide the optimisation of next generation light dark matter direct detection experiments, and this specific research could serve as an incentive to cover other parts of the interaction parameter space of dark matter-electron scattering, in the grand quest of exploring the particle nature of dark matter.

A Mathematical derivations

In this section, a more detailed derivation of the ionization form factor from section 3.2.4 is presented, as well as the expressions for the velocity integral solutions η_2 from section 3.2.6.

A.1 Ionization form factor

The definition of the ionization form factor was given in equation (3.56):

$$|f_{\text{ion}}^{nl}(k',q)|^2 = \frac{4k'^3}{(2\pi)^3}\sum_{l'}\sum_{mm'}\left|\int d^3x\tilde{\psi}^*_{k'l'm'}(\vec{x})\psi_{nlm}(\vec{x})e^{i\vec{q}\cdot\vec{x}}\right|^2. \tag{A.1}$$

The electron wave functions are rewritten in spherical harmonics Y_{lm} and radial wave functions according to

$$\psi_{nlm} = \mathcal{R}_{nl}(r)Y_{lm}(\theta,\phi), \quad \tilde{\psi}_{k'l'm'} = \tilde{\mathcal{R}}_{k'l'}(r)Y_{l'm'}(\theta,\phi). \tag{A.2}$$

The exponential in the form factor integral is also rewritten as a sum over spherical harmonics;

$$e^{i\vec{q}\cdot\vec{r}} = 4\pi\sum_{L=0}^{\infty}\sum_{M=-L}^{L} i^L j_L(qr)Y_{LM}(\theta_q,\phi_q)Y^*_{LM}(\theta,\phi). \tag{A.3}$$

Here $j_L(qr)$ is a spherical Bessel function of order L. Through making use of the mathematical identity

$$\begin{aligned}&\int Y_{lm}(\theta,\phi)Y_{l'm'}(\theta,\phi)Y_{LM}(\theta,\phi)\,\sin\theta\,\mathrm{d}\theta\,\mathrm{d}\phi\\ &= \sqrt{\frac{(2l+1)(2l'+1)(2L+1)}{4\pi}}\begin{pmatrix}l & l' & L\\ 0 & 0 & 0\end{pmatrix}\begin{pmatrix}l & l' & L\\ m & m' & M\end{pmatrix},\end{aligned} \tag{A.4}$$

where the terms in the brackets are Wigner 3j-symbols, the integral over the three spherical harmonics depending on θ and ϕ can be rewritten as:

$$\begin{aligned}|f_{\text{ion}}^{nl}(k',q)|^2 = \frac{4k'^3}{(2\pi)^3}(4\pi)^2\sum_{l'}&\left|\int r^2dr\tilde{\mathcal{R}}^*_{k'l'}(r)\mathcal{R}_{nl}(r)j_L(qr)\right|^2\sum_{L=|l-l'|}^{l+l'}\sum_{mm'M}|Y_{LM}(\theta_q,\phi_q)|^2\\ &\times\frac{(2l+1)(2l'+1)(2L+1)}{4\pi}\begin{bmatrix}l & l' & L\\ 0 & 0 & 0\end{bmatrix}^2\begin{bmatrix}l & l' & L\\ m & m' & -M\end{bmatrix}^2\end{aligned} \tag{A.5}$$

The sums over m, m' and M are performed using the following identities:

$$\sum_{mm'}(L+1)\begin{bmatrix} l & l' & L \\ m & m' & -M \end{bmatrix}^2 = 1, \tag{A.6}$$

$$\sum_{M=-L}^{L} Y^*_{LM}(\theta_q,\phi_q)Y_{LM}(\theta_q,\phi_q) = \frac{2L+1}{4\pi}, \tag{A.7}$$

which yields the final expression for the ionization form factor:

$$|f^{nl}_{\rm ion}(k',q)|^2 = \frac{4k'^3}{(2\pi)^3}\sum_{l'}\sum_{L=|l-l'|}^{l+l'}(2l+1)(2l'+1)(2L+1)\begin{bmatrix} l & l' & L \\ 0 & 0 & 0 \end{bmatrix}^2 \left|\int r^2 dr \tilde{\mathcal{R}}^*_{k'l'}(r)\mathcal{R}_{nl}(r)j_L(qr)\right|^2. \tag{A.8}$$

This is the expression that appears in equation (3.58).

A.2 Solutions of velocity integrals

The second part of the velocity integral in the differential scattering rate, the one that corresponds to the terms in the scattering amplitude that are proportional to v^2, is

$$2\pi\left(\int_{v_{\rm min}}^{v_{\rm esc}-v_E} v^3 dv \int_{-1}^{1} d\cos\theta\, g_\chi(v,\cos\theta) + \int_{v_{\rm esc}-v_E}^{v_{\rm esc}+v_E} v^3 dv \int_{-1}^{\xi(v)} d\cos\theta\, g_\chi(v,\cos\theta)\right), \tag{A.9}$$

with

$$g_\chi(v,\cos\theta) = \frac{1}{K}e^{-(v^2+v_E^2-2vv_E\cos\theta/v_0^2)}, \tag{A.10}$$

and

$$\xi(v) \equiv \frac{v_{\rm esc}^2 - v^2 - v_E^2}{2vv_E}. \tag{A.11}$$

The solution to equation (A.9) is called η_2 and it is divided in the two cases:

(a) $v_{\rm min} < v_{\rm esc} - v_E$

(b) $v_{\rm esc} - v_E < v_{\rm min} < v_{\rm esc} + v_E$.

η_2 is given by

$$\eta_2^{(a)} = \frac{\pi v_0^2}{12 K v_E} - 8(e^{v_{esc}^2/v_0^2} v_E (3v_0^2 + v_E^2 + 3v_{esc}^2) + 6e^{-(v_E+v_{min})^2/v_0^2} v_0^2 \tag{A.12}$$
$$\times (v_E + 2v_E e^{4v_E v_{min}/v_0^2} - v_{min}) + 6e^{-(v_E - v_{min})^2/v_0^2} v_0^2 (v_{min} - v_E)$$
$$+3\sqrt{\pi} v_0 (v_0^2 + 2v_E) \times \left(\text{Erf}\left(\frac{v_E + v_{min}}{v_0} \right) - \text{Erfc}\left(\frac{v_E - v_{min}}{v_0} \right) + 1 \right))$$

$$\eta_2^{(b)} = \frac{\pi v_0^2}{12 K v_E} (e^{v_{esc}^2/v_0^2} (-4(v_e + v_{esc})^3 - 6v_0^2(2v_E + v_{esc}) + 4v_{min}^3) \tag{A.13}$$
$$+3\sqrt{\pi} v_0 (v_0^2 + 2v_E^2) \left(\text{Erf}\left(\frac{v_{esc}}{v_0} \right) + \text{Erf}\left(\frac{v_E - v_{min}}{v_0} \right) \right)$$
$$+6e^{-(v_E - v_{min})^2/v_0^2} v_0^2 (v_E + v_{min})).$$

B Numerical analysis

In figure 15, η_2 from equations (A.12) and (A.13) is plotted as a function of energy deposited to the electron in the scattering process, for a few fixed dark matter masses and transferred momenta. η_2 applies for the terms in the scattering amplitude that are proportional to v^2. Compared to figure 3, showing the velocity integral η_1 that applies for rest of the terms in the scattering amplitude, the behaviour is quite similar. Only higher dark matter masses can induce a scattering process with high energies.

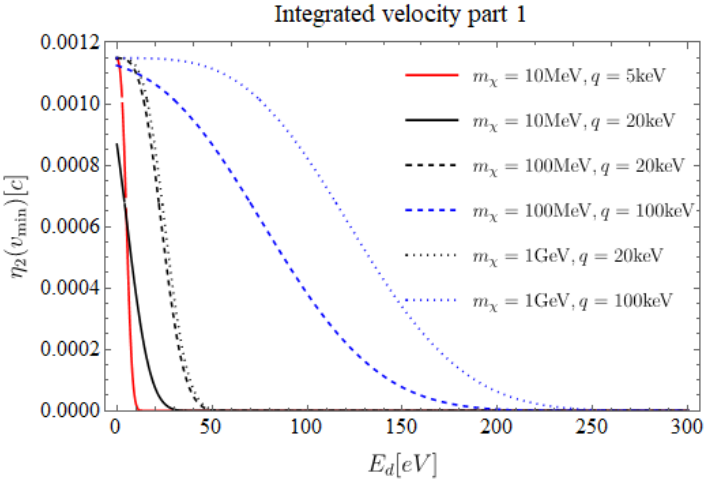

Figure 15: $\eta_2(v_{min}(q, E_d))$ as a function of deposited energy E_d for different dark matter masses and transferred momenta q. η_2 contains all the dark matter velocity information for the terms in $\overline{|\mathcal{M}_{free}|^2} \propto v^2$.

References

[1] Gianfranco Bertone and Dan Hooper. "History of dark matter". In: *Rev. Mod. Phys.* 90.4 (2018), p. 045002. arXiv: 1605.04909 [astro-ph.CO].

[2] Rouven Essig, Jeremy Mardon, and Tomer Volansky. "Direct Detection of Sub-GeV Dark Matter". In: *Phys. Rev.* D85 (2012), p. 076007. arXiv: 1108.5383 [hep-ph].

[3] Bradley J. Kavanagh, Paolo Panci, and Robert Ziegler. "Faint Light from Dark Matter: Classifying and Constraining Dark Matter-Photon Effective Operators". In: *JHEP* 04 (2019), p. 089. arXiv: 1810.00033 [hep-ph].

[4] Farinaldo S. Queiroz, Werner Rodejohann, and Carlos E. Yaguna. "Is the dark matter particle its own antiparticle?" In: *Phys. Rev.* D95.9 (2017), p. 095010. arXiv: 1610.06581 [hep-ph].

[5] B. Kelvin. *Baltimore lectures on molecular dynamics and the wave theory of light*. 1904. URL: https://archive.org/details/baltimorelecture00kelviala/page/n8.

[6] John R. Ellis. "Particle candidates for dark matter". In: *Phys. Scripta* T85 (2000), pp. 221–230. arXiv: astro-ph/9812211 [astro-ph].

[7] Gianfranco Bertone, Dan Hooper, and Joseph Silk. "Particle dark matter: Evidence, candidates and constraints". In: *Phys. Rept.* 405 (2005), pp. 279–390. arXiv: hep-ph/0404175 [hep-ph].

[8] F. Zwicky. "Republication of: The redshift of extragalactic nebulae". In: *General Relativity and Gravitation* 41.1 (Jan. 2009), pp. 207–224. URL: https://doi.org/10.1007/s10714-008-0707-4.

[9] Neal Dalal and Charles R. Keeton. "(Lack of) lensing constraints on cluster dark matter profiles". In: (2003). arXiv: astro-ph/0312072 [astro-ph].

[10] Volker Springel, Carlos S. Frenk, and Simon D. M. White. "The large-scale structure of the Universe". In: *Nature* 440 (2006), p. 1137. arXiv: astro-ph/0604561 [astro-ph].

[11] Joel R. Primack. "Dark matter and structure formation". In: *Midrasha Mathematicae in Jerusalem: Winter School in Dynamical Systems Jerusalem, Israel, January 12-17, 1997*. 1997. arXiv: astro-ph/9707285 [astro-ph].

[12] Wayne Hu. "Wandering in the Background: A Cosmic Microwave Background Explorer". PhD thesis. UNIVERSITY of CALIFORNIA at BERKELEY, 1995.

[13] N. Aghanim et al. "Planck 2018 results. VI. Cosmological parameters". In: (2018). arXiv: 1807.06209 [astro-ph.CO].

[14] ESA. *Space in images: Planck power spectrum*. Mar. 2013. URL: %7Bhttp://esa.int/spaceinimages/Images/2013/03/Planck_Power_Spectrum%7D.

[15] Jose A. R. Cembranos. "Modified gravity and dark matter". In: *Journal of Physics: Conference Series* 718 (May 2016), p. 032004.

[16] Andre Maeder. "Dynamical Effects of the Scale Invariance of the Empty Space: The Fall of Dark Matter?" In: *The Astrophysical Journal* 849.2 (Nov. 2017), p. 158.

[17] M. Milgrom. "A modification of the Newtonian dynamics as a possible alternative to the hidden mass hypothesis". In: *Astrophysical Journal* 270 (Apr. 1983), pp. 365–370.

[18] Pieter van Dokkum et al. "A Second Galaxy Missing Dark Matter in the NGC 1052 Group". In: *Astrophysical Journal* 874.1, L5 (Mar. 2019), p. L5. arXiv: 1901.05973 [astro-ph.GA].

[19] Pieter van Dokkum et al. "A galaxy lacking dark matter". In: *Nature* 555.7698 (Mar. 2018), pp. 629–632. arXiv: 1803.10237 [astro-ph.GA].

[20] Leszek Roszkowski, Enrico Maria Sessolo, and Sebastian Trojanowski. "WIMP dark matter candidates and searches—current status and future prospects". In: *Rept. Prog. Phys.* 81.6 (2018), p. 066201. arXiv: 1707.06277 [hep-ph].

[21] Hsin-Chia Cheng, Jonathan L. Feng, and Konstantin T. Matchev. "Kaluza-Klein dark matter". In: *Phys. Rev. Lett.* 89 (2002), p. 211301. arXiv: hep-ph/0207125 [hep-ph].

[22] R. Bernabei et al. "Final model independent result of DAMA/LIBRA-phase1". In: *Eur. Phys. J.* C73 (2013), p. 2648. arXiv: 1308.5109 [astro-ph.GA].

[23] J. Amaré et al. "First results on dark matter annual modulation from ANAIS-112 experiment". In: (2019). arXiv: 1903.03973 [astro-ph.IM].

[24] E. Aprile et al. "Dark Matter Search Results from a One Ton-Year Exposure of XENON1T". In: *Phys. Rev. Lett.* 121.11 (2018), p. 111302. arXiv: 1805.12562 [astro-ph.CO].

[25] Cláudio Frederico Pascoal da Silva. "Dark Matter Searches with LUX". In: *Proceedings, 52nd Rencontres de Moriond on Very High Energy Phenomena in the Universe: La Thuile, Italy, March 18-25, 2017*. 2017, pp. 199–209. arXiv: 1710.03572 [hep-ex].

[26] Giorgio Arcadi et al. "The waning of the WIMP? A review of models, searches, and constraints". In: *Eur. Phys. J.* C78.3 (2018), p. 203. arXiv: 1703.07364 [hep-ph].

[27] V.S. Berezinsky. "Cosmology of the gravitino as the lightest supersymmetric particle". In: *Physics Letters B* 261.1 (1991), pp. 71–75. URL: http://www.sciencedirect.com/science/article/pii/037026939191327R.

[28] Laura Covi et al. "Axinos as dark matter". In: *JHEP* 05 (2001), p. 033. arXiv: hep-ph/0101009 [hep-ph].

[29] Kalliopi Petraki and Raymond R. Volkas. "Review of asymmetric dark matter". In: *Int. J. Mod. Phys.* A28 (2013), p. 1330028. arXiv: 1305.4939 [hep-ph].

[30] Alexander Kusenko. "Sterile neutrinos: The Dark side of the light fermions". In: *Phys. Rept.* 481 (2009), pp. 1–28. arXiv: 0906.2968 [hep-ph].

[31] Jason Kumar. "Indirect Detection of Sub-GeV Dark Matter Coupling to Quarks". In: *Phys. Rev.* D98.11 (2018), p. 116009. arXiv: 1808.02579 [hep-ph].

[32] Rouven Essig et al. "Constraining Light Dark Matter with Diffuse X-Ray and Gamma-Ray Observations". In: *JHEP* 11 (2013), p. 193. arXiv: 1309.4091 [hep-ph].

[33] J. P. Lees et al. "Search for Invisible Decays of a Dark Photon Produced in e^+e^- Collisions at BaBar". In: *Phys. Rev. Lett.* 119.13 (2017), p. 131804. arXiv: 1702.03327 [hep-ex].

[34] Hideki Miyake. "Belle II Experiment: Status and Physics Prospects". In: *Nucl. Part. Phys. Proc.* 303-305 (2018), pp. 20–24.

[35] C. Bird, Robert V. Kowalewski, and M. Pospelov. "Dark matter pair-production in b —> s transitions". In: *Mod. Phys. Lett.* A21 (2006), pp. 457–478. arXiv: hep-ph/0601090 [hep-ph].

[36] Rouven Essig et al. "Constraining Light Dark Matter with Low-Energy e^+e^- Colliders". In: *JHEP* 11 (2013), p. 167. arXiv: 1309.5084 [hep-ph].

[37] Teresa Marrodán Undagoitia and Ludwig Rauch. "Dark matter direct-detection experiments". In: *J. Phys.* G43.1 (2016), p. 013001. arXiv: 1509.08767 [physics.ins-det].

[38] Paolo Gondolo. "Recoil momentum spectrum in directional dark matter detectors". In: *Phys. Rev.* D66 (2002), p. 103513. arXiv: hep-ph/0209110 [hep-ph].

[39] Rouven Essig et al. "Direct Detection of sub-GeV Dark Matter with Semiconductor Targets". In: *JHEP* 05 (2016), p. 046. arXiv: 1509.01598 [hep-ph].

[40] P. Agnes et al. "Constraints on Sub-GeV Dark-Matter–Electron Scattering from the DarkSide-50 Experiment". In: *Phys. Rev. Lett.* 121.11 (2018), p. 111303. arXiv: 1802.06998 [astro-ph.CO].

[41] Rouven Essig et al. "First Direct Detection Limits on sub-GeV Dark Matter from XENON10". In: *Phys. Rev. Lett.* 109 (2012), p. 021301. arXiv: 1206.2644 [astro-ph.CO].

[42] D. S. Akerib et al. "Results of a Search for Sub-GeV Dark Matter Using 2013 LUX Data". In: *Phys. Rev. Lett.* 122.13 (2019), p. 131301. arXiv: 1811.11241 [astro-ph.CO].

[43] R. Agnese et al. "First Dark Matter Constraints from a SuperCDMS Single-Charge Sensitive Detector". In: *Phys. Rev. Lett.* 121.5 (2018). [erratum: Phys. Rev. Lett.122,no.6,069901(2019)], p. 051301. arXiv: 1804.10697 [hep-ex].

[44] The SENSEI Collaboration et al. "SENSEI: First Direct-Detection Constraints on sub-GeV Dark Matter from a Surface Run". In: *Physical Review Letters* 121 (Mar. 2018).

[45] Ramamurti Shankar. *Principles of Quantum Mechanics*. Second. Springer, 1994.

[46] J. Barranco et al. "Distinguishing Dirac and Majorana neutrinos with astrophysical fluxes". In: (2017). arXiv: 1704.01549 [hep-ph].

[47] M. Peskin and D. Schroeder. *An Introduction to Quantum Field Theory*. Advanced Book Program, 1995.

[48] Eugenio Del Nobile, Marco Nardecchia, and Paolo Panci. "Millicharge or Decay: A Critical Take on Minimal Dark Matter". In: *JCAP* 1604.04 (2016), p. 048. arXiv: 1512.05353 [hep-ph].

[49] Sacha Davidson, Steen Hannestad, and Georg Raffelt. "Updated bounds on millicharged particles". In: *JHEP* 05 (2000), p. 003. arXiv: hep-ph/0001179 [hep-ph].

[50] BungeC.F, J.A.Bunge, and J.A. Barrientos. "Roothaan-Hartree-Fock Ground-State Atomic Wave Functions: Slater-Type Orbital Expansions and Expectation Values for Z = 2-54". In: *Atomic Data and Nuclear Data Tables* 53.1 (1993), pp. 113–162.

[51] Hans A. Bethe and Edwin E. Salpeter. *Quantum Mechanics of One- and Two-Electron Atoms*. Springer, 1977.

[52] E. Aprile et al. "XENON100 Dark Matter Results from a Combination of 477 Live Days". In: *Phys. Rev.* D94.12 (2016), p. 122001. arXiv: 1609.06154 [astro-ph.CO].

[53] Riccardo Catena and Piero Ullio. "A novel determination of the local dark matter density". In: *JCAP* 1008 (2010), p. 004. arXiv: 0907.0018 [astro-ph.CO].

[54] Pijushpani Bhattacharjee et al. "Sizing-up the WIMPs of Milky Way : Deriving the velocity distribution of Galactic Dark Matter particles from the rotation curve data". In: *Phys. Rev.* D87 (2013), p. 083525. arXiv: 1210.2328 [astro-ph.GA].

[55] Jason Wyenberg and Ian M. Shoemaker. "Mapping the neutrino floor for direct detection experiments based on dark matter-electron scattering". In: *Phys. Rev.* D97.11 (2018), p. 115026. arXiv: 1803.08146 [hep-ph].